

PAPER • OPEN ACCESS

Centrality determination in heavy-ion collisions with the LHCb detector

To cite this article: The LHCb collaboration *et al* 2022 *JINST* **17** P05009

View the [article online](#) for updates and enhancements.

You may also like

- [Observation of Gravitational Waves from Two Neutron Star–Black Hole Coalescences](#)

R. Abbott, T. D. Abbott, S. Abraham et al.

- [Diving below the Spin-down Limit: Constraints on Gravitational Waves from the Energetic Young Pulsar PSR J0537-6910](#)

R. Abbott, T. D. Abbott, S. Abraham et al.

- [Searches for Continuous Gravitational Waves from Young Supernova Remnants in the Early Third Observing Run of Advanced LIGO and Virgo](#)

R. Abbott, T. D. Abbott, S. Abraham et al.



ECS Membership = Connection

ECS membership connects you to the electrochemical community:

- Facilitate your research and discovery through ECS meetings which convene scientists from around the world;
- Access professional support through your lifetime career;
- Open up mentorship opportunities across the stages of your career;
- Build relationships that nurture partnership, teamwork—and success!

Join ECS!

Visit electrochem.org/join



RECEIVED: November 4, 2021

ACCEPTED: March 29, 2022

PUBLISHED: May 5, 2022

Centrality determination in heavy-ion collisions with the LHCb detector



The LHCb collaboration

E-mail: garcia@l1r.in2p3.fr

ABSTRACT: The centrality of heavy-ion collisions is directly related to the created medium in these interactions. A procedure to determine the centrality of collisions with the LHCb detector is implemented for lead-lead collisions at $\sqrt{s_{NN}} = 5$ TeV and lead-neon fixed-target collisions at $\sqrt{s_{NN}} = 69$ GeV. The energy deposits in the electromagnetic calorimeter are used to determine and define the centrality classes. The correspondence between the number of participants and the centrality for the lead-lead collisions is in good agreement with the correspondence found in other experiments, and the centrality measurements for the lead-neon collisions presented here are performed for the first time in fixed-target collisions at the LHC.

KEYWORDS: Pattern recognition, cluster finding, calibration and fitting methods; Performance of High Energy Physics Detectors; Simulation methods and programs

ARXIV EPRINT: [2111.01607](https://arxiv.org/abs/2111.01607)



© 2022 CERN for the benefit of the LHCb collaboration. Published by IOP Publishing Ltd on behalf of Sissa Medialab. Original content from this work may be used under the terms of the [Creative Commons Attribution 4.0 licence](https://creativecommons.org/licenses/by/4.0/). Any further distribution of this work must maintain attribution to the author(s) and the title of the work, journal citation and DOI.

<https://doi.org/10.1088/1748-0221/17/05/P05009>

2022 JINST 17 P05009

Contents

1	Introduction	1
2	The LHCb detector	2
3	Glauber model	3
4	Data	4
4.1	PbPb collisions	5
4.2	PbNe collisions	5
5	Centrality determination	7
5.1	Methodology	7
5.1.1	Events simulation	8
5.1.2	Fit model	9
5.1.3	Fit to the PbPb collision data	10
5.1.4	Fit to the PbNe collision data	14
5.1.5	Centrality classes	16
5.2	Results	16
6	Systematic uncertainties	19
6.1	Bin-width dependence	19
6.2	Hadronic cross-section uncertainty	19
6.3	Fit uncertainty	20
6.4	Uncertainty from the Negative Binomial Distribution	20
6.5	Total systematic uncertainties	20
7	Conclusions	22
The LHCb collaboration		25

1 Introduction

In the context of heavy-ion collision, centrality is a quantity of relevance since it is directly related to the overlap region between the two nuclei in a collision. Centrality gives access to the number of nucleons participating in the collision (N_{part}) as well as the number of binary nucleon-nucleon collisions (N_{coll}), which are useful quantities to compare data from different experiments, different collision systems and to theoretical calculations. The centrality of a collision, defined as the percentile of the total inelastic nucleus-nucleus collision cross-section, is characterised by the impact parameter (b) between the two nuclei, *i.e.* the distance between their centres in the plane transverse to the beam

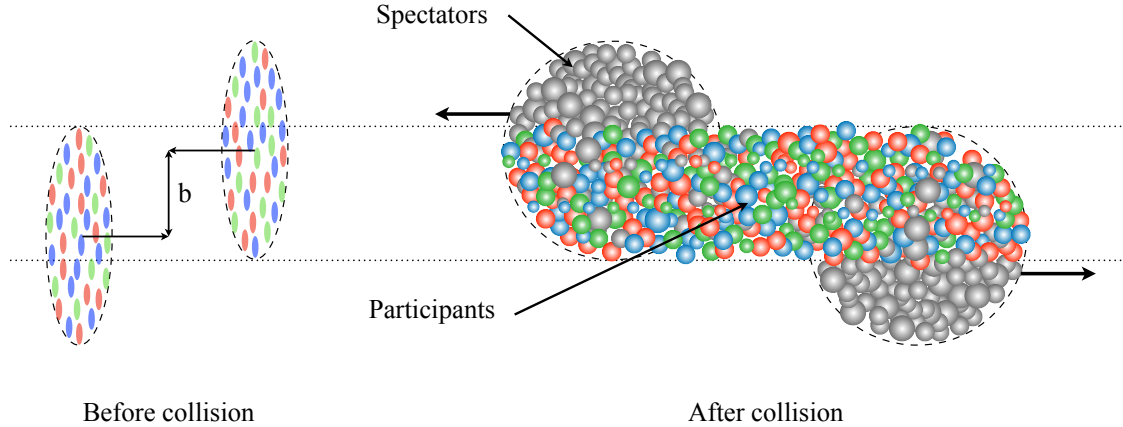


Figure 1. A schematic view of a heavy-ion collision. The impact parameter b is shown as well as the spectator nucleons and the participant nucleons.

axis. The impact parameter defines the overlap region of the nuclei and thus influences also the size and shape of the resulting medium. A schematic view of a heavy-ion collision is shown in figure 1.

The geometry of the collision is related to the number of participating nucleons and the number of binary nucleon-nucleon collisions. These quantities are not directly accessible and hence need to be derived from the data recorded during the collisions by making use of other quantities that scale approximately with the number of participating nucleons, such as the outgoing particle multiplicity. For this purpose, a Glauber model [1] is often used and the particle production modelled with the aid of a Negative Binomial Distribution (NBD).

This paper presents the centrality determination with the LHCb detector for lead-lead (PbPb) collisions at a centre-of-mass energy $\sqrt{s_{\text{NN}}} = 5 \text{ TeV}$, which is in agreement with results obtained by the ALICE [2, 3], ATLAS [4] and CMS [5] collaborations, and the first centrality determination in fixed-target mode at the LHC, for lead-neon (PbNe) collisions at $\sqrt{s_{\text{NN}}} = 69 \text{ GeV}$. After introducing the LHCb detector in section 2, the Glauber model and the assumptions it relies on are described in section 3. The datasets used are presented in section 4 followed by the centrality determination procedure with its results in section 5. Finally, the study of systematic uncertainties is shown in section 6.

2 The LHCb detector

The LHCb detector [6, 7] is a single-arm forward spectrometer covering the pseudorapidity range $2 < \eta < 5$, designed for the study of particles containing b or c quarks. The detector includes a high-precision tracking system consisting of a silicon-strip vertex detector (VELO) surrounding the beam interaction region with two pile-up (PU) stations upstream from the interaction point, a large-area silicon-strip detector located upstream of a dipole magnet with a bending power of about 4 Tm, and three stations of silicon-strip detectors and straw drift tubes placed downstream of the magnet. The tracking system provides a measurement of the momentum of charged particles with a relative uncertainty that varies from 0.5% at low momentum to 1.0% at $200 \text{ GeV}/c$. The minimum distance of a track to a primary vertex (PV), is measured with a resolution of $(15 + 29/p_{\text{T}}) \mu\text{m}$, where p_{T} is the component of the momentum transverse to the beam, in GeV/c . Different types of

charged hadrons are distinguished using information from two ring-imaging Cherenkov detectors. Photons, electrons and hadrons are identified by a calorimeter system consisting of scintillating-pad (SPD) and pre-shower detectors, an electromagnetic (ECAL) and a hadronic (HCAL) calorimeter. Muons are identified by a system composed of alternating layers of iron and multiwire proportional chambers. The online event selection is performed by a trigger, which consists of a hardware stage, based on information from the calorimeter and muon systems, followed by a software stage, which applies a full event reconstruction.

A gas-injection system for beam-gas interactions (SMOG) [8] is installed in the LHCb detector, which gives the unique possibility of injecting a low pressure noble gas and collecting fixed-target collisions (proton-nucleus or nucleus-nucleus).

3 Glauber model

The centrality of a nucleus-nucleus collision is related to the overlap region between the nuclei where the nucleons are colliding. In practice, the particles produced by the collisions are not originating purely from hadronic interactions between the nuclei. At LHC energies, the electromagnetic field generated by the heavy ions leads to large QED process cross-sections, contaminating the hadronic cross section. Those QED processes are studied in ultra-peripheral collisions (UPC) where the impact parameter of the collision is larger than the sum of the radii of the nuclei; they can also significantly contaminate the hadronic cross-section in the most peripheral collisions [9]. Therefore, a model is needed to isolate the hadronic part and subsequently define the centrality classes. The most common approach in heavy-ion physics to model the collisions of two nuclei is to consider the transverse shapes of the nuclei. This shape, *i.e.* the nuclear density, is described by a two-parameter Fermi distribution (2pF), also known as Woods-Saxon distribution [1], for each nuclear species considered, defined as

$$\rho(r) dr = \rho_0 \frac{1 + w \frac{r^2}{R^2}}{1 + \exp(\frac{r-R}{a})} dr, \quad (3.1)$$

where r stands for the radial distance from the centre of the nucleus, ρ_0 is a normalisation factor, and R corresponds to the nuclear radius, which is approximately the radial extension of the bulk of the nucleus. The diffusivity a describes how abruptly the density falls at the edge of the nucleus. The last parameter, w , is used to describe nuclei whose maximum density is reached at a radius $r > 0$. The values of these parameters are taken from other experiments, typically involving lepton-nucleus collisions and other types of nuclear spectroscopy [10, 11]. The 2pF distribution can be seen in figure 2 with parameters $R = 6$ fm, $a = 0.5$ fm and $w = 0$ for illustration.

The Glauber model is generally approached in two ways, the optical Glauber model and the Monte Carlo (MC) Glauber model. The two colliding nuclei are labelled A and B . In the optical model, it is considered that nucleons from projectile A see the target B as a continuous distribution, which is described by an analytical function, and vice versa. This is also called the optical limit approximation. Subsequently, the overlap area, the number of participating nucleons and the number of binary nucleon-nucleon collisions can be obtained analytically.

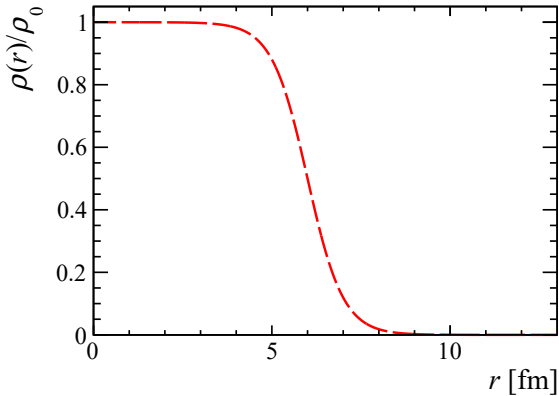


Figure 2. The 2pF density distribution ρ as a function of the radius r . Here w has been set to 0, $R = 6$ fm and $a = 0.5$ fm.

On the other hand, in the MC Glauber model, the calculation is performed through a MC method where nucleons from each nucleus A and B are generated as hard spheres¹ and are placed around the respective centres of the nuclei following the 2pF distributions. Then a random impact parameter b is sampled from the distribution $d\sigma/db = 2\pi b$. Finally, the MC simulation of the collision of the two nuclei is performed under the following assumptions:

- nucleus-nucleus collisions are considered to be a superposition of several independent nucleon-nucleon collisions;
- nucleons are treated as hard spheres moving in straight lines all along the process, even if they have undergone a collision;
- nucleons have a geometrical transverse cross-section ($\sigma_{\text{NN}}^{\text{inel}}$) and two nucleons collide if the transverse distance between their centres is $d < \sqrt{\sigma_{\text{NN}}^{\text{inel}}/\pi}$.

The distribution and average values of the number of participating nucleons N_{part} , of binary nucleon-nucleon collisions N_{coll} and other quantities, are obtained using the simulated collisions.

The Glauber model has two relevant external inputs, the nucleon-nucleon inelastic cross-section $\sigma_{\text{NN}}^{\text{inel}}$ and the spatial distribution given by the 2pF distribution with its parameters R , a and w . The cross-section is obtained from a phenomenological parametrisation tuned on data, using measurements from a broad range of energies from ~ 20 GeV to ~ 60 TeV, given by $\sigma_{\text{NN}}^{\text{inel}}(s) = A + B \ln^2(s)$, with $A = 25.0 \pm 0.9$ and $B = 0.146 \pm 0.004$ [13]. The optical approach describes fairly well the collision process but does not completely capture the physics of the total cross-section and leads to distortions in the estimation of N_{part} and N_{coll} compared to the estimation made with the MC approach [1]. Therefore, in the following, the MC Glauber model is used.

4 Data

For the centrality determination a minimum bias (MB) data sample is needed, that is, data that have the minimum possible number of selections applied, to not bias the sample.

¹There is a variation of the model that can also take into account the sub-nucleonic dynamics called Glauber-Gribov [12].

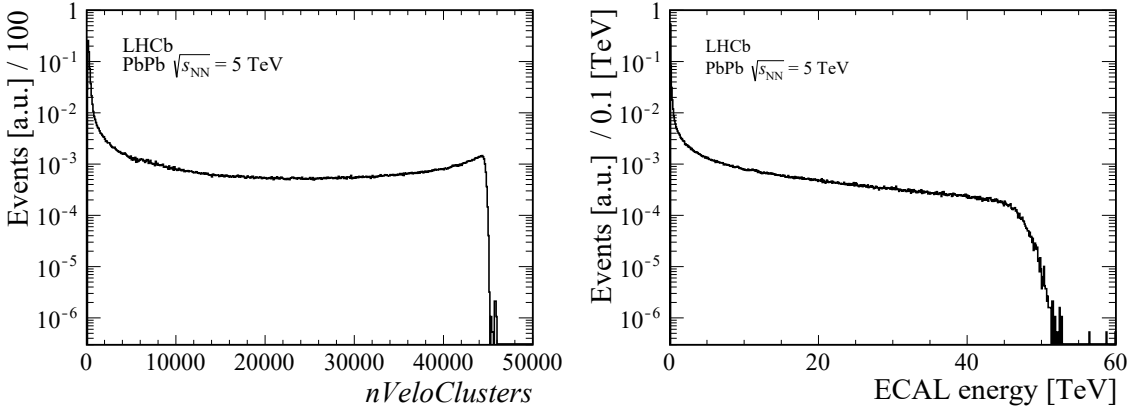


Figure 3. (left) Number of Velo clusters and (right) energy deposited in the ECAL in PbPb collisions. The distribution of the Velo clusters exhibits a peak structure with a sharp fall at 45 000 clusters. This is related to the total number of readout channels in the Velo, leading to saturation for high occupancy events.

4.1 PbPb collisions

For PbPb collisions, the sample used for this analysis corresponds to the data recorded in a special run of the 2018 PbPb data-taking period, at a centre-of-mass energy per nucleon of $\sqrt{s_{\text{NN}}} = 5 \text{ TeV}$. The MB trigger requirement was to record at least one track in the Velo. Throughout the data-taking period, PbPb collisions were recorded in parallel with fixed-target PbNe collisions, between Pb beams and atoms of Ne injected in the Velo with the SMOG system. However, for this particular MB data sample, no gas was injected. The resulting distribution of the number of Velo clusters ($n_{\text{VeloClusters}}$), which are clustered energy deposits in the Velo stations, and of the energy deposited in the ECAL are shown in figure 3.

4.2 PbNe collisions

The PbNe data sample corresponds to a MB sample from the whole data-taking period when gas was injected during the 2018 LHC PbPb data-taking runs. The PbNe collisions occur at a centre-of-mass energy per nucleon of $\sqrt{s_{\text{NN}}} = 69 \text{ GeV}$ where the Ne atoms act as a fixed target. In order to avoid contamination from PbPb collisions that were recorded simultaneously, only events for those bunch crossings where a filled bunch from the incoming Pb beam does not cross a filled bunch from the opposing Pb beam are selected. There is some residual contamination in the data sample and extra selections are applied to increase the fraction of PbNe collisions.

The different topology of the PbPb and PbNe events allows to disentangle these two types of events by setting an upper limit on the number of clusters in the PU stations, which are located upstream from the nominal interaction point. Since the PbNe collisions are all boosted downstream, *i.e.* towards the detector, naturally a low number of clusters in the PU stations is expected. On the other hand, since PbPb collisions are symmetric, a larger number of clusters in the PU stations is observed for these collisions.

Another source of contamination are the beam-gas collisions that take place far upstream. Since the injected gas can travel up to 20 m in either direction from the nominal interaction point, the

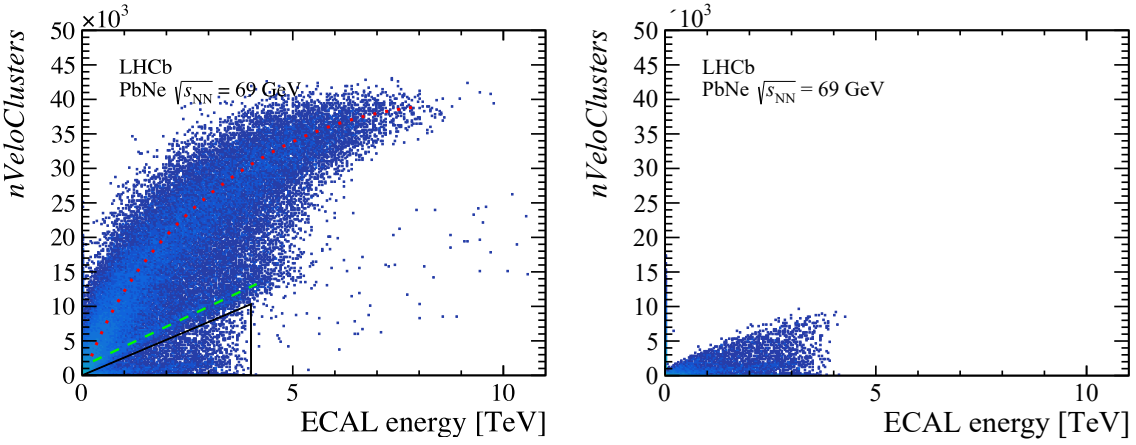


Figure 4. Number of VELO clusters as a function of ECAL energy for PbNe events without any requirement (left) and without any cluster in the PU stations (right). The dotted red line indicates the population which corresponds to the very upstream events, the dashed green line indicates the population which corresponds to ghost PbPb collisions and the solid black lines enclose the PbNe collisions of interest which present no clusters in the PU stations.

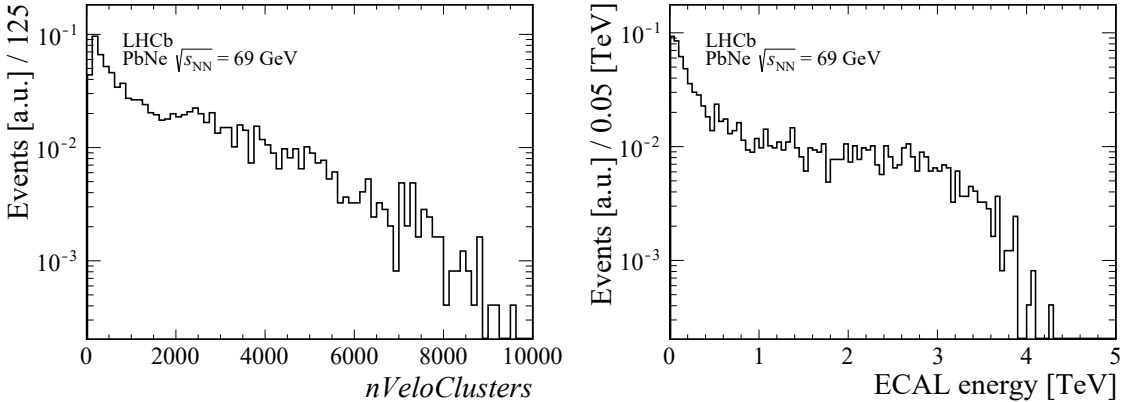


Figure 5. (left) Number of VELO clusters and (right) energy deposited in the ECAL from PbNe collisions.

incoming Pb beam can undergo interactions with the gas before arriving into the VELO tank. These events can produce forward particles, hitting the PU stations and depositing energy in the detector.

To ensure a high enough purity of PbNe collisions in the sample, events with clusters in the PU stations are rejected. The effect of this requirement can be seen in figure 4. On the left, three different populations can be seen, the high-slope population which corresponds to the very upstream events (dotted red line), the middle-slope population which corresponds to ghost PbPb collisions (dashed green line),² and finally the continuum which corresponds to the PbNe collisions of interest which present no clusters in the PU stations (enclosed by solid black lines).

Only the central-region PbNe events are used in what follows, *i.e.* events whose primary vertex is located in the range $z_{\text{PV}} \in [-200, 200]$ mm. The number of VELO clusters and distribution of ECAL energy are shown in figure 5.

²Ghost PbPb collisions occur when Pb ions in the downstream beam escape their nominal bunches within the beam and travel with empty outgoing bunches, leading to collisions when there should be none.

Overall, for PbNe, the following selections are applied:

- Select events where a filled bunch from the incoming Pb beam does not cross a filled bunch from the opposing Pb beam.
- Select events with no activity in the PU stations.
- Select events with the primary vertex located in the range $z_{\text{PV}} \in [-200, 200]$ mm.

5 Centrality determination

Any observable that scales monotonically with impact parameter could be used for classification according to centrality. In practice, the reach in centrality possible with the tracking detectors of LHCb is limited by the performance of these detectors at high track multiplicities. In the case of PbPb collisions this means that the VELO information cannot be used for this purpose, since its sensors saturate under these conditions as seen in the rightmost part of the plot on the left of figure 3. In contrast, the ECAL has the advantage of not saturating even in the most central collisions, as can be seen in the right plot of figure 3. In the case of PbNe collisions, the VELO does not saturate but still cannot be used for the centrality determination, since the relevant events take place all along the length of the VELO. This means that the measured VELO multiplicity depends on the position of the collisions along the beam axis. For this reason the energy deposited in the ECAL is used for the multiplicity determination of both PbPb and PbNe collisions.

Centrality classes are defined as quantiles of the inelastic PbPb or PbNe cross-section. The data contain contributions to the deposited energy in the ECAL from both hadronic and electromagnetic origin. Thus, the energy spectrum cannot be used straightforwardly to define the desired quantiles for centrality. To estimate the hadronic component, a MC Glauber model [13] is used to simulate the colliding nuclei, and from the resulting quantities such as b , N_{coll} or N_{part} , the expected observable can be constructed, which is in this case the energy deposited in the ECAL. The parameters of the model are then tuned to fit the ECAL energy distribution from the data. Finally, the centrality quantiles are defined from the simulated distribution that corresponds only to the hadronic part of the interaction. Geometric quantities from the Glauber MC can then be mapped to the data for each centrality class.

5.1 Methodology

In this section the simulation of the events is described first, then the generation of the simulated ECAL energy distribution and the steps to fit it to the data are explained. Once the fit has been performed, the simulated distribution is split into centrality classes based on the fraction of the total hadronic distribution integral, and the geometric variables of each class are mapped to the measured events falling in the same class.

Table 1. Parameters for the 2pF density function. In the case of Ne the nuclear radius R is taken from refs. [10, 11] while the diffusivity a is set to a commonly used empirical value [14–16].

	R [fm]	a [fm]
^{208}Pb		
p	6.68	0.45
n	6.69	0.56
^{20}Ne	3.01	0.54

5.1.1 Events simulation

The first step is to simulate the collisions using the TGLAUBERMC software from ref. [13].³ The parameters for the 2pF density function are listed in table 1. In all cases, the parameter w is assumed to be equal to 0.

One million PbPb collisions are simulated using the corresponding nucleon-nucleon cross-section $\sigma_{\text{NN}}^{\text{inel}} = 67.6$ mb for a centre-of-mass energy of $\sqrt{s_{\text{NN}}} = 5$ TeV, and one million PbNe collisions were simulated using the corresponding nucleon-nucleon cross-section $\sigma_{\text{NN}}^{\text{inel}} = 35.4$ mb for a centre-of-mass energy of $\sqrt{s_{\text{NN}}} = 69$ GeV. The uncertainty on the nucleon-nucleon cross-sections is considered in the corresponding systematic uncertainty treatment in section 6.2.

The N_{part} and N_{coll} values of every simulated collision are then computed. With these numbers, the number of ancestors N_{anc} is defined as

$$N_{\text{anc}} = f \times N_{\text{part}} + (1 - f) \times N_{\text{coll}}, \quad (5.1)$$

which effectively scales with the number of sources of particle production, with a relative weight for the participating nucleons and the number of collisions. This is motivated by the fact that the particle multiplicity is expected to scale with N_{part} when soft processes dominate and to scale with N_{coll} when hard processes dominate [17–21]. Below a centre-of-mass energy of about 100 GeV soft processes are expected to dominate. The parameter f determines the fraction of soft processes that contribute to the particle production and has to be determined with a fit. In figure 6, the distributions of N_{part} , N_{coll} and N_{anc} in simulation are displayed with, as an example, $f = 0.751$ for the PbPb case.

To get the distribution of particles originating from the collision, N_{anc} is convoluted with an NBD which has been extensively used to model particle production and has been shown to be a reasonable approach at diverse energy and rapidity regimes [22–26]. The NBD is given in its discrete form by

$$P_{p,k}(n) = \frac{(n+k-1)!}{n!(k-1)!} p^k (1-p)^n, \quad (5.2)$$

with $p = (\frac{\mu}{k} + 1)^{-1}$, where μ and k are parameters related to the mean and spread of the NBD respectively, and n is the number of particles that are produced and deposited energy in the ECAL. Since there are N_{anc} particle sources for each nucleus-nucleus collision, each producing particles

³For this work, in the Glauber software the Pb nucleus was specified as Pbprnw, which considers slightly different distributions for protons and neutrons in the nucleus, and a reweighting of the nucleons positions to make the centre-of-mass coincide with the nominal position of the nucleus.

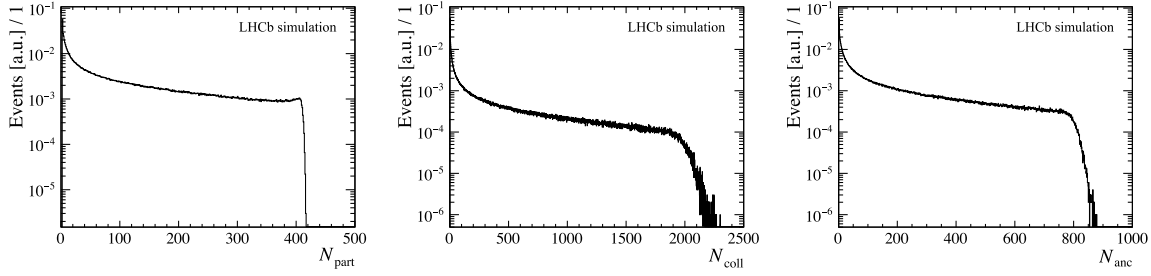


Figure 6. Distribution of (left) N_{part} , (middle) N_{coll} and (right) N_{anc} from the MC Glauber model for PbPb. For this N_{anc} distribution, a value of $f = 0.751$ was used.

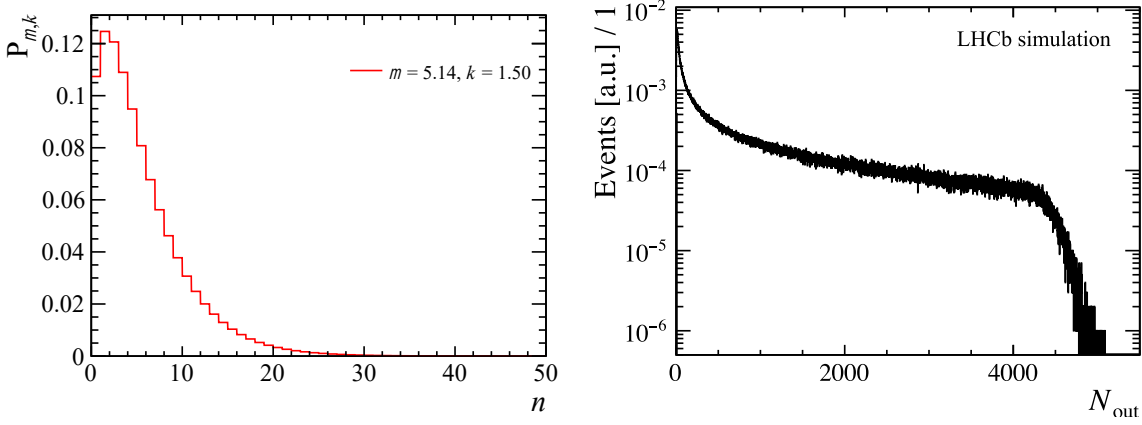


Figure 7. (left) Negative Binomial Distribution and (right) distribution of the number of outgoing particles from the MC Glauber model in PbPb collisions at $\sqrt{s_{\text{NN}}} = 5$ TeV.

following an NBD, the NBD is sampled N_{anc} times to get the particle multiplicity distribution. Figure 7 illustrates the NBD function and the result after sampling it N_{anc} times for each event to obtain the distribution of the number of outgoing particles (N_{out}) which deposit energy in the ECAL.

The mean energy per particle in the ECAL is assumed to come mainly from π^0 decays. The π^0 spectrum is approximated with the charged pion spectrum seen in data in MB pp collisions at 5 TeV. The value for the mean energy deposited per particle in the ECAL is found to be $\langle E^{\text{PbPb}} \rangle = 10.4$ GeV. The pion energy deposit distribution in pp collisions and the simulated ECAL energy distribution for PbPb can be seen in figure 8.

The same procedure is repeated for the PbNe case. However, since there are no pp data at $\sqrt{s_{\text{NN}}} = 69$ GeV, $p\text{Ne}$ collisions from the 2015 data-taking period at this centre-of-mass energy are used. The value for the mean energy found is $\langle E^{\text{PbNe}} \rangle = 10.4$ GeV. This value is consistent with the one found for PbPb, but this is compensated by a much lower number of particles produced in the collisions.

5.1.2 Fit model

The parameter k is linked to the width of the NBD distribution. The ALICE collaboration uses a value $k = 1.6$ [27] in their analysis. A comparison is made between PbPb simulated distributions varying k between 1.0 and 2.0 while everything else is kept constant. It is found that there is no

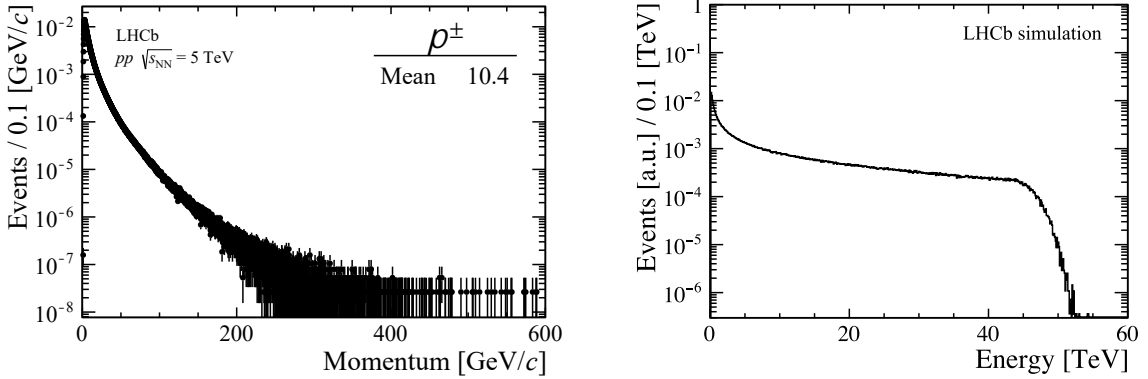


Figure 8. Pion energy deposit in the ECAL from $\sqrt{s_{NN}} = 5 \text{ TeV}$ pp collisions (left). Simulated distribution of the energy deposited in the ECAL for $PbPb$ collisions. A mean energy deposition per particle of $\langle E_{PbPb} \rangle = 10.4 \text{ GeV}$ is considered (right).

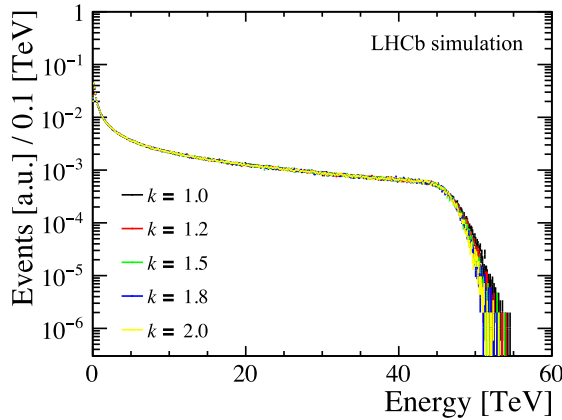


Figure 9. Resulting $PbPb$ simulated energy distribution in the ECAL for $k \in [1.0, 2.0]$.

significant dependence on this parameter. The resulting distributions can be seen in figure 9. For this reason the parameter k was fixed to $k = 1.5$ to be in the middle of the explored range. Finally the model has only two free parameters, f from eq. (5.1) and μ from the NBD.

5.1.3 Fit to the $PbPb$ collision data

To fit the simulated distribution to the data a χ^2 function on both distributions is minimised. It is defined as

$$\chi^2 = \sum_{i \in \text{bins}} \frac{(E_i - O_i)^2}{E_i}, \quad (5.3)$$

where E_i and O_i are the expected and observed values for the i^{th} bin, *i.e.* the simulated and measured values for a given energy bin, assuming the values are counts with Poissonian errors. As previously mentioned, in order to avoid a possible contamination at low energy of electromagnetic origin, the fitting range is chosen to be from 2 to 52 TeV. The MC Glauber energy distribution is normalised to the data in the energy range of 5 to 15 TeV to avoid the extremes of the distributions.

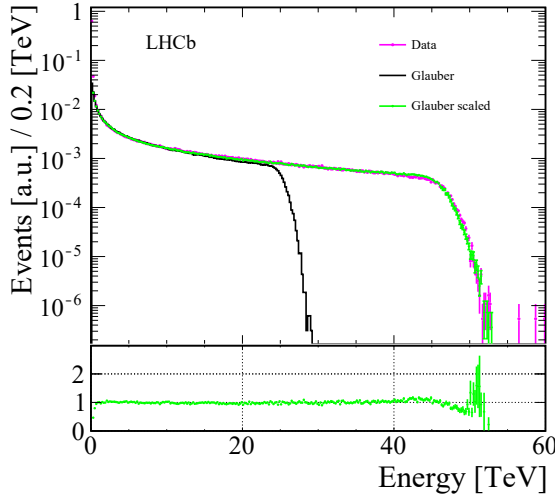


Figure 10. ECAL energy distribution comparison between PbPb data and MC glauber. The black histogram corresponds to the simulated distribution with $f = 0.9$ which is then rescaled by H_s (green dots) to match the data and compare the right shoulders. For the entire process μ was fixed to 3.85.

The fit procedure is delicate since the variables f and μ are highly correlated as they both modulate the horizontal reach of the distribution: μ is related to the mean value of the NBD, and thus the higher the value of μ , the higher the number of particles produced per collision and consequently the more energy is deposited in the ECAL. On the other hand, f controls how alike the final distribution is to the distributions of N_{part} or N_{coll} , which have a different reach on the x -axis. For the same reason f controls the shape of the right shoulder, which helps disentangle f from μ .

In the first step μ is fixed to a test value, $\mu = 3.85$, and the similarity between the right shoulder of the data and the simulated distributions is evaluated for 1000 different values of f ranging from 0 to 1. For this procedure the simulated distribution is horizontally stretched to match the data by a factor H_s defined as

$$H_s = \frac{E_s^{\text{Data}}}{E_s^{\text{Glauber}}}, \quad (5.4)$$

where E_s^{Data} is the energy of the right shoulder of the data distribution, and E_s^{Glauber} is the energy of the right shoulder of the simulated distribution. This scaling procedure is shown in figure 10, where the data have been normalised to 1. For this step, the χ^2 is computed from 35 to 52 TeV to only consider the right shoulder. The resulting values for the χ^2 as a function of f can be seen in figure 11.

The minimum of the χ^2 is found to be at $f = 0.83$. This result is taken as a reference to reduce the range in f for the subsequent grid search. The allowed range for f is set to be $[0.60, 0.93]$, from which the range for μ is chosen to be $[3.7, 9.0]$. A grid of 100×100 is defined and the χ^2 is computed from 2 to 52 TeV at every point of the grid. The result of this grid search can be seen in figure 12.

The best fit is not associated to the point of the grid with the lowest value, since this is prone to be affected by the fluctuations from the random NBD sampling. Instead the χ^2 map from figure 12 is considered and the minimum parametrised by f and by μ separately. In order to get

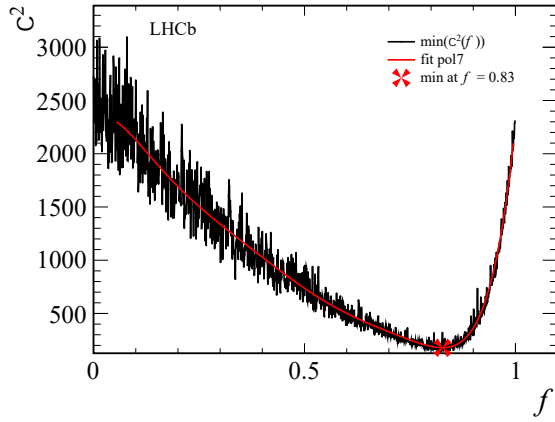


Figure 11. The χ^2 values for 1000 steps in $f \in [0, 1]$ for the PbPb case. The χ^2 values have been fitted by a 7th degree polynomial whose minimum is at $f = 0.83$.

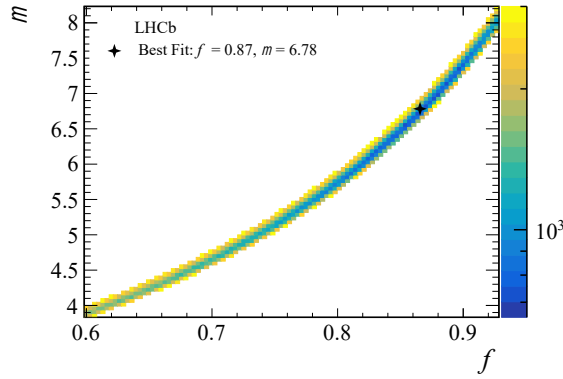


Figure 12. The χ^2 map for the coarse grid search in $f \in [0.60, 0.93]$ and $\mu \in [3.7, 9.0]$ for the PbPb case. The best fit corresponds to the values $f = 0.866$ and $\mu = 6.778$.

the parametrisation as a function of f , the minimum of the χ^2 as a function of μ in bins of f is found. Like this, the value of the minimum in each slice along μ (at fixed f) is assigned to the corresponding value of f . The same is done for the μ dependence. Consequently, for all values of f and μ the f -parametrised minimum and μ -parametrised minimum are constructed. In figure 13 the parametrisations as a function of f and μ are shown and an example slice is displayed to illustrate the process. From this procedure, the best fit is found at $(f, \mu) = (0.866, 6.778)$ with a $\chi^2/\text{ndf} = 3.025$, which is the one shown in figure 12. The number of points on the grid is not limiting the precision on the result.

Finally another grid search is performed with the same amount of points but on a narrower range, namely $f \in [0.79, 0.92]$ and $\mu \in [5.7, 7.9]$. The resulting χ^2 map is shown in figure 14. Two results are shown as a best fit. The star is the nominal value, whereas the cross is obtained by using an alternative method where the slice is fitted to obtain the minimum of this fit. The best fits found are $(f, \mu) = (0.869, 6.814)$ with $\chi^2/\text{ndf} = 2.82$ and $(f, \mu) = (0.869, 6.853)$ with $\chi^2/\text{ndf} = 2.83$. These best fits correspond to the star and the cross on figure 14 respectively. Since the goodness of fit is virtually the same for the two best fits, the one which is kept is $(f, \mu) = (0.869, 6.814)$.

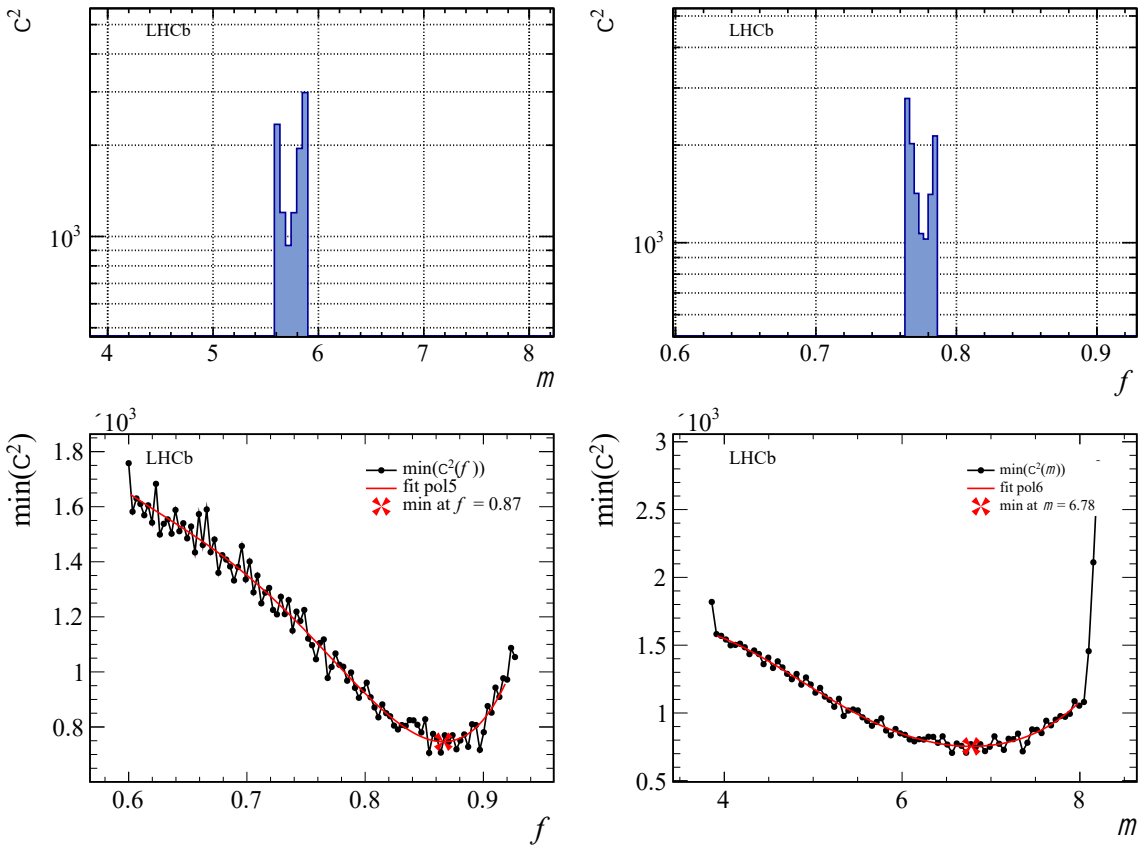


Figure 13. The top plots show a slice for (left) $f = 0.798$ and for (right) $\mu = 5.45$. From each slice, the minimum of the histogram is kept. The bottom plots show the result of doing this for all values of f and μ , that is, the f -parametrised minimum (left) and the μ -parametrised minimum (right) for the PbPb case using the coarse grid. These are fitted by a 5th and 6th degree polynomial respectively whose minima are at $f = 0.866$ and $\mu = 6.778$.

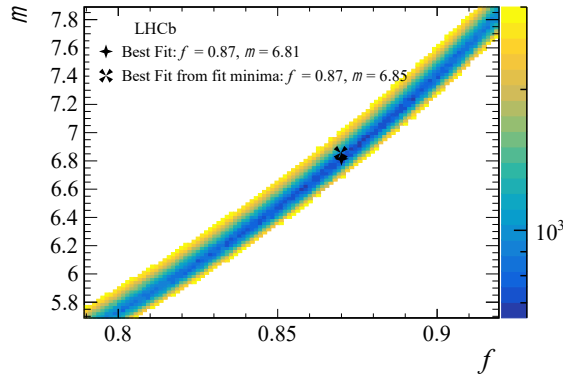


Figure 14. Map of χ^2 values for the fine grid search in $f \in [0.79, 0.92]$ and $\mu \in [5.7, 7.9]$ for the PbPb case. The two shown best fits correspond to the results from two different methods (see text).

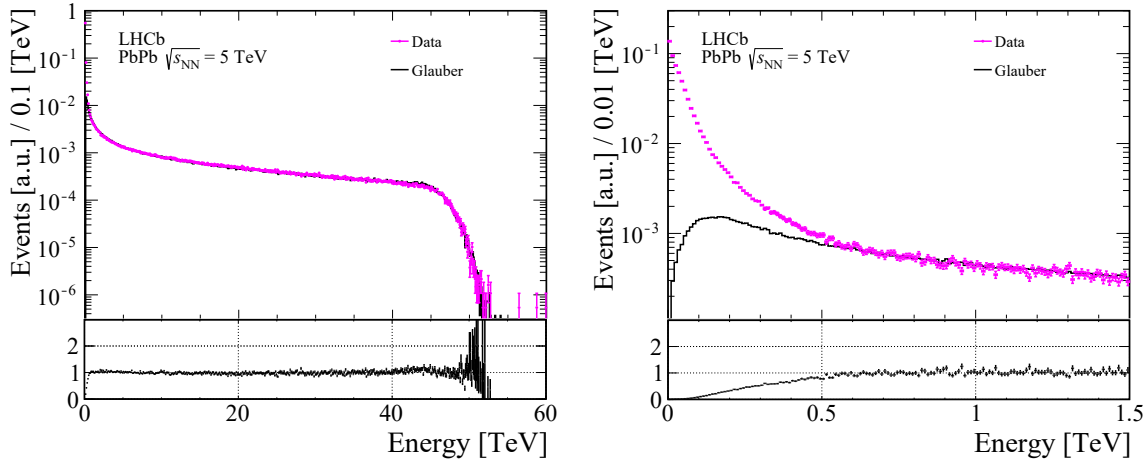


Figure 15. Final fit of the simulated energy distribution to the data for PbPb collisions. The best fit found is $(f, \mu) = (0.869, 6.814)$ with a corresponding $\chi^2/\text{ndf} = 2.82$. The right figure corresponds to a close-up view of the left figure.

The final result of the fit can be seen in figure 15. On the right plot of figure 15 a zoom of the low-energy part of the distribution is displayed, where the discrepancy between the MC Glauber and the data, due to the presence of events of electromagnetic origin, becomes clear. This will be addressed in more detail in section 5.2. This region below 0.5 TeV is well outside the fitting range, which starts at 2 TeV. The Glauber model, with its parameters obtained from a fit to the data, can thus be used to define the centrality classes in PbPb collision data.

5.1.4 Fit to the PbNe collision data

The same χ^2 function from eq. (5.3) is used to evaluate the goodness of fit of the Glauber MC to the data for PbNe collisions. The fitting range is chosen to be from 0.5 to 3.9 TeV in order to avoid possible contamination from electromagnetic origin present at low energy. The Glauber MC energy distribution is normalised to the data in the energy range of 0.5 to 2 TeV to not consider the tails of the distributions, even in the case where f takes on the extreme values.

Since in this scenario the shape of the energy distribution at high energy is not as characteristic as it is for PbPb, the approach of trying to fit f first cannot be applied, and the allowed range remains $f \in [0.0, 1.0]$, since there is still sensitivity to the contributions of N_{part} or N_{coll} . The range in μ is chosen accordingly to be $\mu \in [1.0, 3.4]$. A grid of 200×200 is defined in the previously mentioned ranges and the χ^2 is computed at every point of the grid. The result of this grid search can be seen in figure 16.

To find the best fits shown in figure 16, the same approach described for the PbPb case is used. The values of f and μ -parametrised minima are obtained by taking the minimum value for every slice (first method, star in figure 16), and by fitting each slice and getting the minimum of the fit (second method, cross in figure 16). However, in the following step only the μ -parametrised minima are fit to get the optimal μ whereas for the f -parametrised minima, the f value where the χ^2 is minimum is picked without fit. This is because the f -parametrised distributions show a steep decrease as f approaches one, and fitting a function around that region is difficult. The best fit

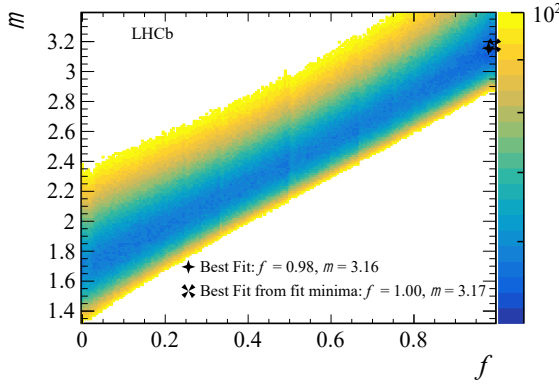


Figure 16. Map of χ^2 values for the coarse grid search in $f \in [0.0, 1.0]$ and $\mu \in [1.0, 3.4]$ for the PbNe case. The two best fits shown correspond to the results of two different methods described in the text.

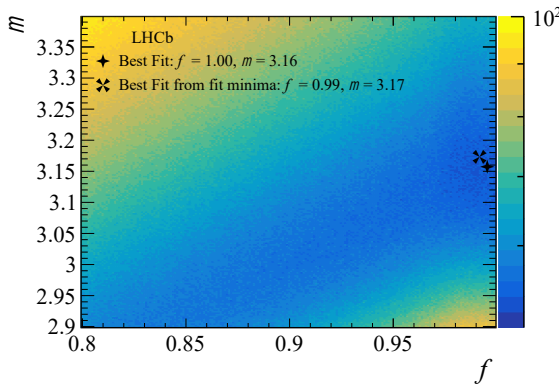


Figure 17. Map of χ^2 values for the fine grid search in $f \in [0.8, 1.0]$ and $\mu \in [2.9, 3.4]$ for the PbNe case. The two shown best fits correspond to the results from two different methods described in the text.

is found at $(f, \mu) = (0.980, 3.156)$ with a $\chi^2/\text{ndf} = 1.039$, and at $(f, \mu) = (0.995, 3.174)$ with a $\chi^2/\text{ndf} = 1.031$. These best fits are shown in figure 16 by a star and a cross, respectively.

Finally another grid search is performed where the same amount of points is used but on a narrower range, namely $f \in [0.8, 1.0]$ and $\mu \in [2.9, 3.4]$. From this grid, the best fits are found at $(f, \mu) = (0.996, 3.157)$ with a $\chi^2/\text{ndf} = 1.026$, and at $(f, \mu) = (0.992, 3.173)$ with a $\chi^2/\text{ndf} = 1.031$, computed using the same methods described above. The resulting χ^2 map and the best fits are shown in figure 17 by a star and a cross, respectively. Since the goodness of fit is virtually the same for all best fits in the coarse and fine grid, the one kept is the one which results in the smallest χ^2 value, that is, $(f, \mu) = (0.996, 3.157)$.

The final result of the fit can be seen in figure 18. On the right plot, a zoom of the low-energy part of the distribution is shown, where the discrepancy between the Glauber MC and the data, due to the presence of events of electromagnetic origin, becomes clear. This region below 0.1 TeV is well below the fitting range, which starts at 0.5 TeV.

The fact that f is close to one (hence $N_{\text{anc}} \sim N_{\text{part}}$) is due to the fact that, below a nucleon-nucleon centre-of-mass energy of about 100 GeV, the particle production is dominated by soft processes, which scale geometrically, as mentioned in section 5.1.1.

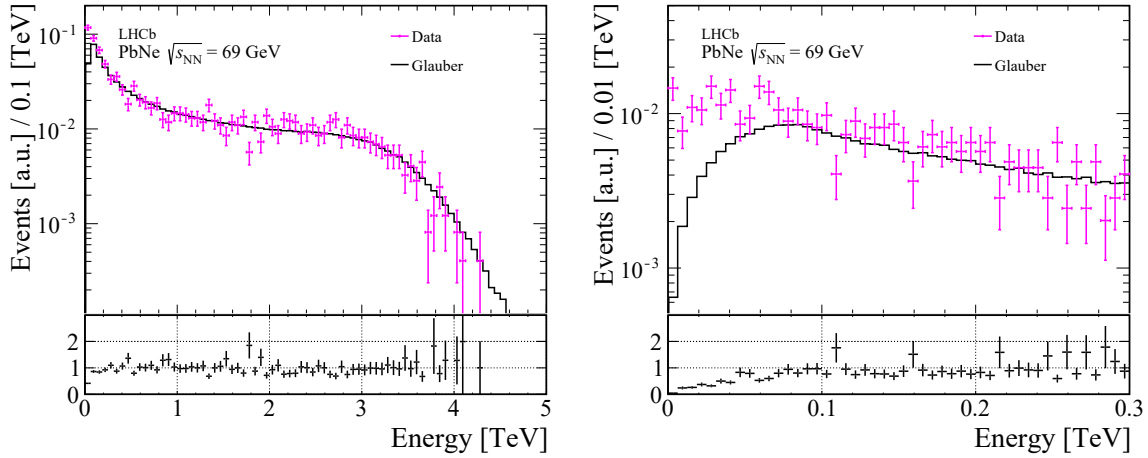


Figure 18. Final fit of the simulated energy distribution to the data for PbNe collisions. The best fit found is $(f, \mu) = (0.996, 3.157)$ with a corresponding $\chi^2/\text{ndf} = 1.026$. The right figure corresponds to a close-up view of the left figure.

5.1.5 Centrality classes

After obtaining the simulated distribution of energy deposited in the ECAL, which corresponds only to the hadronic contribution, the distribution can be divided into centrality classes. To determine the ECAL energy boundary values for each class, the simulated distribution is integrated from a value of deposited energy to infinity, until a starting value is found giving a percentage of the total integral. Defining I_T as the total integral of the energy distribution, the ECAL energy requirement for any percentage p of centrality, would be the value of E_p such that

$$(p \times 10^{-2}) I_T = \int_{E_p}^{\infty} \frac{dN}{dE} dE. \quad (5.5)$$

Similarly, as an example, the centrality class (10 – 20)% would correspond to the events depositing an energy E such that $E_{20} < E < E_{10}$.

5.2 Results

The centrality classification of the MB dataset of PbPb collisions in percentile intervals of 10%, with the requirements in energy obtained as in the previously described procedure, is shown in figure 19 as well as the b , N_{part} and N_{coll} distributions for each class obtained from the Glauber MC model. For each class a mean number is estimated for each of the quantities of interest, together with their corresponding standard deviations. The same distributions for the PbNe case can be seen in figure 20.

In this way, one can define as many classes as desired and of arbitrary width in percentiles. The values of the geometric quantities for each class, as well as the corresponding energy requirements, can be seen in table 2 for PbPb and in table 3 for PbNe. Ten classes are shown for each case.

The PbNe results, when compared to the PbPb case, exhibit a larger uncertainty in the values of the geometrical quantities. This limited precision is an effect of the system size which is much smaller in the case of PbNe, and not a result of the use of the ECAL to estimate centrality. If the centrality classes were defined purely from the Glauber model by applying sharp cuts in the b

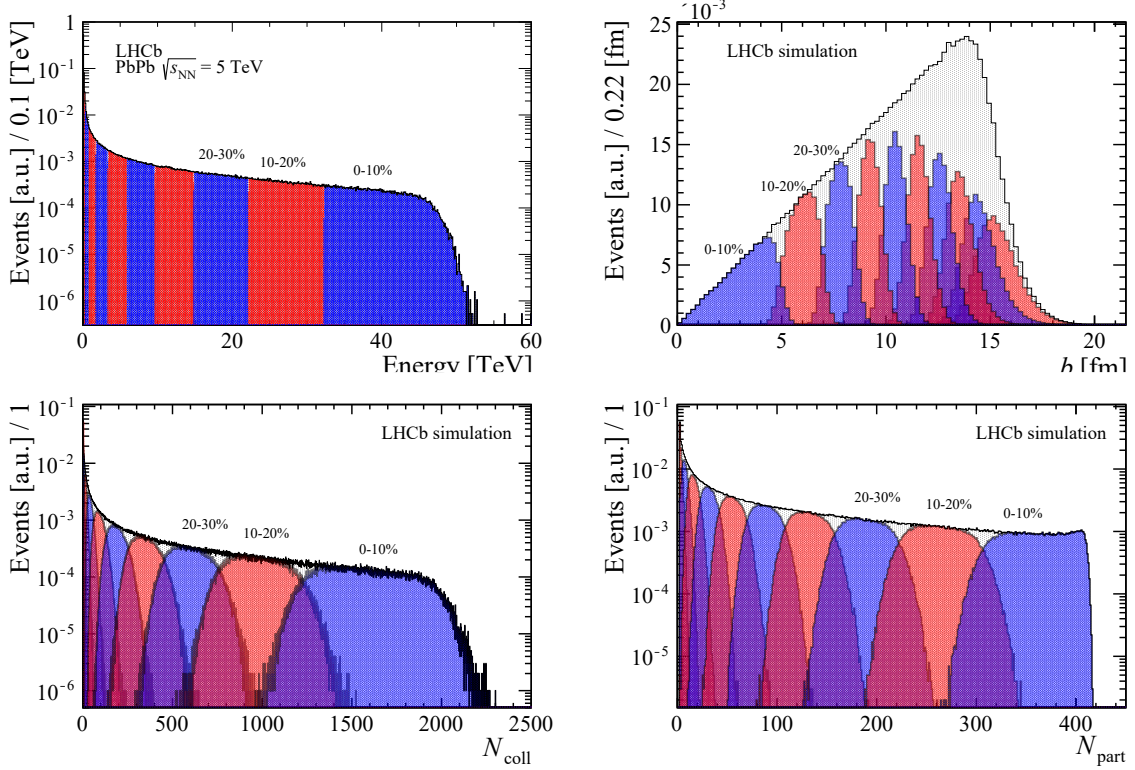


Figure 19. (top left) Classification of events from PbPb data according to the defined centrality classes, distribution of the (top right) impact parameter, (bottom left) N_{coll} and (bottom right) N_{part} quantities for the corresponding centrality classes.

Table 2. Geometric quantities (N_{part} , N_{coll} and b) of PbPb collisions for centrality classes defined from a Glauber MC model fitted to the data. The classes correspond to sharp cuts in the energy deposited in the ECAL. Here σ stands for the standard deviation of the corresponding distributions.

Centrality %	E [GeV]	N_{part}	$\sigma_{N_{\text{part}}}$	N_{coll}	$\sigma_{N_{\text{coll}}}$	b	σ_b
100–90	0–310	2.9	1.2	1.8	1.2	15.4	1.0
90–80	310–800	7.0	2.9	5.8	3.1	14.6	0.9
80–70	800–1750	15.9	4.8	16.4	7.0	13.6	0.7
70–60	1750–3360	31.3	7.1	41.3	14.7	12.6	0.6
60–50	3360–5900	54.7	10.0	92.6	27.7	11.6	0.5
50–40	5900–9630	87.5	13.3	187.5	46.7	10.5	0.5
40–30	9630–14860	131.2	16.9	345.5	71.6	9.2	0.5
30–20	14860–22150	188.0	21.5	593.9	105.2	7.8	0.6
20–10	22150–32280	261.8	27.1	972.5	151.9	6.0	0.7
10–0	32280– ∞	357.2	32.2	1570.3	236.8	3.3	1.2

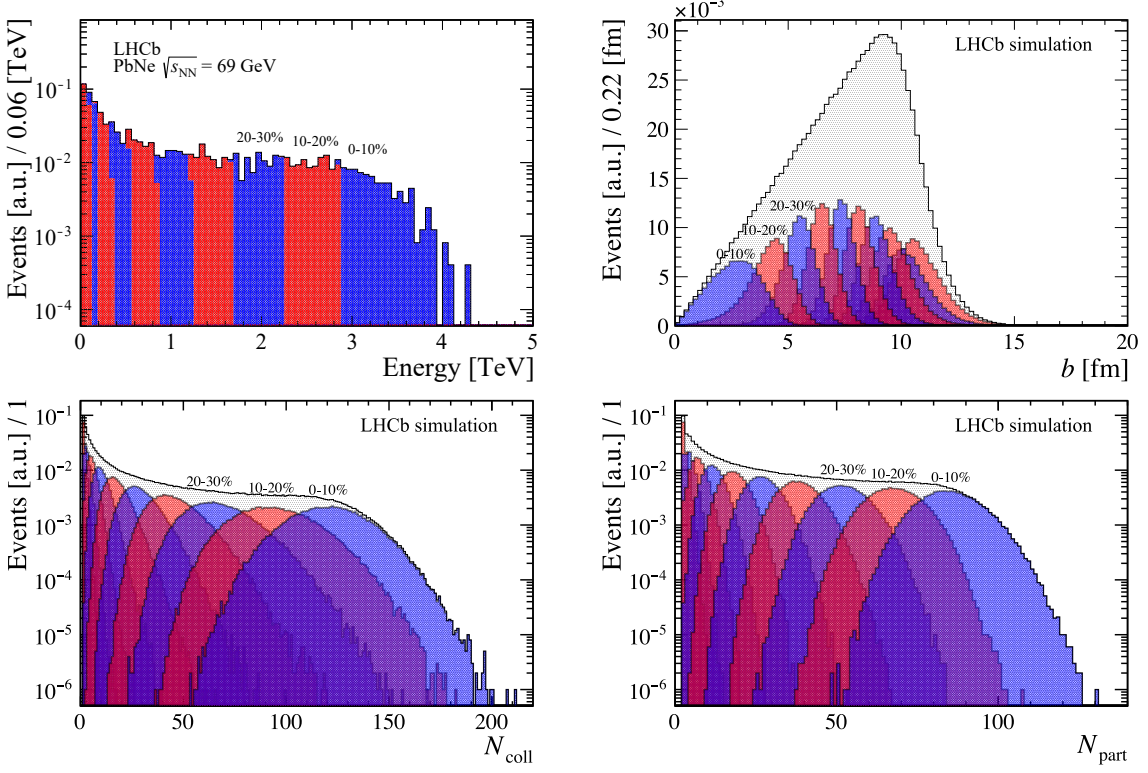


Figure 20. (top left) Classification of events from PbNe data according to the defined centrality classes, distribution of the (top right) impact parameter, (bottom left) N_{coll} and (bottom right) N_{part} values for the corresponding centrality classes.

Table 3. Geometric quantities (N_{part} , N_{coll} and b) of PbNe collisions for centrality classes defined from a MC Glauber model fitted to the data. The classes correspond to sharp cuts in the energy deposited in the ECAL. Here σ stands for the standard deviation of the corresponding distributions.

Centrality %	E [GeV]	N_{part}	$\sigma_{N_{\text{part}}}$	N_{coll}	$\sigma_{N_{\text{coll}}}$	b	σ_b
100–90	0–94	2.5	0.8	1.4	0.7	10.9	1.1
90–80	94–184	3.9	1.6	2.7	1.5	10.4	1.0
80–70	184–324	6.8	2.4	5.2	2.4	9.7	0.9
70–60	324–533	11.3	3.2	9.7	3.8	9.0	0.8
60–50	532–828	17.9	4.2	17.3	5.9	8.2	0.7
50–40	828–1213	26.7	5.2	29.0	8.7	7.4	0.6
40–30	1213–1690	38.0	6.3	45.6	12.3	6.5	0.7
30–20	1690–2250	51.7	7.5	67.8	16.1	5.4	0.8
20–10	2250–2879	67.3	8.3	94.1	18.9	4.1	1.0
10–0	2879– ∞	84.8	9.5	120.4	18.6	2.7	1.1

distribution, the same large overlaps in the N_{coll} and N_{part} distributions would be found, without ever including the ECAL in the procedure.

One important caveat is that at low energy the dominating events are of electromagnetic nature or from UPC. Because of this, it is important to exclude in the analyses the energy region where there is a sizeable contamination from these events. If no further selection has been applied to reject UPC events, its contamination in PbPb events will be below 5% at energies higher than 585 GeV, that is at centralities lower than 84%, and for PbNe at energies higher than 98.9 GeV, that is at centralities lower than 89%.

To determine this threshold, the data are compared to the fitted Glauber MC as in the right plot of figure 15. The point from which the two distributions match is found by computing a centred mean of the data over MC ratio around each bin. For a given bin n , in the case of PbPb, the ratio of data over MC is computed for bins $n - 1$, n and $n + 1$, and averaged. For PbNe, the ratio of data over MC is computed for the five precedent bins, for bin n , and for the five subsequent bins, and averaged. When this ratio is below a chosen tolerance of 1.05 (meaning 5% contamination of UPC events) for three consecutive bins, the centre of the bin of lower energy is chosen as the energy threshold. If UPC events were identified and rejected, then this limit, of 84% for PbPb or 89% for PbNe, could be increased to include more peripheral events.

The results in the PbPb case are in very good agreement with the results obtained by the ALICE [2, 3], ATLAS [4] and CMS [5] collaborations at the same centre-of-mass energy. The PbNe results correspond to the first centrality measurements in fixed-target collisions at the LHC.

6 Systematic uncertainties

In the given centrality classes with fixed deposited energy boundaries, the uncertainties on the geometric quantities, like the mean values of N_{part} , N_{coll} and b , are assessed. The previously found energy selections are kept, but the systematic uncertainties are quantified on the geometric properties. In what follows, the systematic uncertainties are reported in tables of ten classes of ten percentiles each.

6.1 Bin-width dependence

To find the boundary values of the ECAL energy bins, an integration procedure is performed on the histogram of the simulated energy deposition per event. The larger the bins, the less precise the percentile of events in the energy bins can be determined.

A binning scheme of 6000 bins is used, which has an average miss percentage of 0.04% for the PbPb case and 0.02% for PbNe. Since each percentile corresponds to a 1% interval, an average miss of 0.04% means that on average 4% of the events of one percentile “migrate” to the class immediately below in energy. The effect on the geometric quantities is estimated and the results are stored for every percentile and N_{part} , N_{coll} and b .

6.2 Hadronic cross-section uncertainty

One of the main ingredients for the Glauber MC model is the nucleon-nucleon cross-section. For PbPb at a centre-of-mass energy of $\sqrt{s_{\text{NN}}} = 5$ TeV, it corresponds to $\sigma_{\text{NN}}^{\text{inel}} = 67.6 \pm 0.6$ mb, where the uncertainty comes from the data driven parametrisation described in ref. [13]. For PbNe at a centre-of-mass energy of $\sqrt{s_{\text{NN}}} = 69$ GeV, the nucleon-nucleon cross-section corresponds to

$\sigma_{\text{NN}}^{\text{inel}} = 35.4 \pm 0.9$ mb. To quantify the effect this uncertainty has in the geometric properties, the simulated energy distribution is generated from a Glauber MC simulation made with $\sigma_{\text{NN}}^{\text{inel}} + 1\sigma$ and with $\sigma_{\text{NN}}^{\text{inel}} - 1\sigma$ for each collision system. Then the centrality classes are defined with these new distributions and the effect on the mean values for N_{part} , N_{coll} and b is taken as the associated systematic uncertainty.

6.3 Fit uncertainty

One of the most important steps in the process of determining centrality is the choice of the parameters f and μ . From section 5.1.3, for PbPb there are three best fits that are found, and four for PbNe. These best fits are used to compute the systematic uncertainties due to the choice of a given set of (f, μ) for PbPb and then for PbNe.

In order to compute the uncertainty the Glauber MC energy distribution is generated with the different sets of values. For both PbPb and PbNe separately, the centrality classes are defined for each set of best fits and finally the resulting mean values of the geometric quantities (N_{part} , N_{coll} and b) are compared between the best fits that were not kept and the one that was kept as the definitive best fit.

The precision at which the mean energy deposited per particle is determined in the ECAL does not affect the final result, since any variation of this value would be compensated by the value of μ found. Thus the uncertainty on this energy is absorbed into the uncertainty due the choice of a given set of parameters (f, μ) .

6.4 Uncertainty from the Negative Binomial Distribution

The NBD sampling introduces statistical fluctuations that affect directly the observed χ^2 value when comparing the Glauber MC simulation and the data. This effect is noticeable even when looking at the same point of the (f, μ) parameter space. To estimate how these fluctuations affect the final computed geometric quantities, ten simulated energy distributions are generated with the same best fit parameters and the geometric quantities are computed for all of them.

For each percentile, the standard deviation for N_{part} , N_{coll} and b is computed and used as uncertainty. As before, this is done separately for PbPb and for PbNe.

6.5 Total systematic uncertainties

These uncertainties are added together in quadrature to obtain the total uncertainty for each centrality class. The result can be seen in table 4 for ten classes for the PbPb case, and in table 5 for the PbNe case. Table 6 shows the relative uncertainty from each source considered with respect to the $\langle N_{\text{part}} \rangle$ value for the centralmost class (10–0%) and for the class 80–70%.

The uncertainties on the geometric quantities in both cases are dominated by the systematic uncertainties, as expected. In the PbPb case, the dominant one is the uncertainty due to the binning effect, while in the PbNe case, the dominant one is the uncertainty due to the binning effect in more peripheral collisions (centrality higher than 50%) and the uncertainty due to the hadronic cross-section uncertainty for more central events (centrality lower than 50%).

Table 4. Total uncertainties for the geometric quantities (N_{part} , N_{coll} and b) of PbPb collisions for centrality classes defined from a MC Glauber model fit to the data. The statistical and systematic uncertainties are added in quadrature, denoted by σ , with the statistical component being largely negligible in the combination in all bins.

Centrality %	$N_{\text{part}} \pm \sigma$	$N_{\text{coll}} \pm \sigma$	$b \pm \sigma$
100–90	2.9 ± 0.5	1.8 ± 0.3	15.41 ± 2.96
90–80	7.0 ± 0.8	5.8 ± 0.6	14.56 ± 1.80
80–70	15.9 ± 0.6	16.4 ± 0.7	13.59 ± 0.52
70–60	31.3 ± 0.7	41.3 ± 0.9	12.61 ± 0.28
60–50	54.6 ± 1.1	92.6 ± 2.0	11.59 ± 0.24
50–40	87.5 ± 1.0	187.5 ± 2.4	10.47 ± 0.14
40–30	131.2 ± 1.2	345.5 ± 3.9	9.23 ± 0.08
30–20	188.0 ± 1.5	593.9 ± 6.6	7.80 ± 0.06
20–10	261.8 ± 1.8	972.5 ± 10.4	6.02 ± 0.04
10–0	357.2 ± 1.7	1570.3 ± 15.6	3.31 ± 0.01

Table 5. Total uncertainties for the geometric quantities (N_{part} , N_{coll} and b) of PbNe collisions for centrality classes defined from a MC Glauber model fit to the data. The statistical and systematic uncertainties are added in quadrature, denoted by σ , with the statistical component being largely negligible in the combination in all bins.

Centrality %	$N_{\text{part}} \pm \sigma$	$N_{\text{coll}} \pm \sigma$	$b \pm \sigma$
100–90	2.5 ± 0.1	1.4 ± 0.0	10.85 ± 0.33
90–80	3.9 ± 0.2	2.7 ± 0.1	10.37 ± 0.41
80–70	6.8 ± 0.3	5.2 ± 0.2	9.69 ± 0.34
70–60	11.3 ± 0.3	9.7 ± 0.3	8.95 ± 0.22
60–50	17.9 ± 0.3	17.3 ± 0.4	8.19 ± 0.09
50–40	26.7 ± 0.3	29.0 ± 0.6	7.38 ± 0.06
40–30	38.0 ± 0.6	45.6 ± 1.1	6.48 ± 0.08
30–20	51.7 ± 0.6	67.8 ± 1.6	5.44 ± 0.03
20–10	67.3 ± 0.8	94.1 ± 2.3	4.14 ± 0.03
10–0	84.8 ± 1.0	120.4 ± 3.0	2.67 ± 0.03

Table 6. Uncertainty from each source considered relative to $\langle N_{\text{part}} \rangle$ of the classes 10–0% and 80–70%, for the PbPb and PbNe case.

	Centrality class	Bin-width	Hadronic cross-section	Fit	NBD
PbPb	80–70%	3.96%	0.44%	0.38%	0.25%
	10–0%	0.46%	0.08%	0.06%	0.03%
PbNe	80–70%	3.53%	0.74%	0.29%	0.29%
	10–0%	0.54%	1.01%	0.12%	0.06%

7 Conclusions

A procedure to determine the centrality in PbPb collisions at $\sqrt{s_{\text{NN}}} = 5$ TeV and in PbNe collisions at $\sqrt{s_{\text{NN}}} = 69$ GeV with the LHCb detector is implemented. The distributions of measured energy deposits in the ECAL are fitted to obtain the parameters f and μ , needed for the determination of the number of ancestors and the NBD respectively, leading to the Glauber simulated distribution. After the fit is performed, the simulated distribution is divided in percentiles, which are delimited by sharp energy boundaries obtained by integrating the distribution. These energy selections allow to classify the data into the same percentiles and subsequently the geometric quantities from the Glauber MC model can be mapped to the real data. The obtained centrality classification is limited to the 84% (89%) most central PbPb (PbNe) events, avoiding the region with large contamination from ultra-peripheral collisions. The correspondence between the results obtained for the PbPb collisions is in good agreement with the results from the ALICE, ATLAS and CMS experiments, and the centrality measurements for the PbNe collisions presented here are the first performed in fixed-target collisions at the LHC.

Acknowledgments

We express our gratitude to our colleagues in the CERN accelerator departments for the excellent performance of the LHC. We thank the technical and administrative staff at the LHCb institutes. We acknowledge support from CERN and from the national agencies: CAPES, CNPq, FAPERJ and FINEP (Brazil); MOST and NSFC (China); CNRS/IN2P3 (France); BMBF, DFG and MPG (Germany); INFN (Italy); NWO (Netherlands); MNiSW and NCN (Poland); MEN/IFA (Romania); MSHE (Russia); MICINN (Spain); SNSF and SER (Switzerland); NASU (Ukraine); STFC (United Kingdom); DOE NP and NSF (U.S.A.). We acknowledge the computing resources that are provided by CERN, IN2P3 (France), KIT and DESY (Germany), INFN (Italy), SURF (Netherlands), PIC (Spain), GridPP (United Kingdom), RRCKI and Yandex LLC (Russia), CSCS (Switzerland), IFIN-HH (Romania), CBPF (Brazil), PL-GRID (Poland) and NERSC (U.S.A.). We are indebted to the communities behind the multiple open-source software packages on which we depend. Individual groups or members have received support from ARC and ARDC (Australia); AvH Foundation (Germany); EPLANET, Marie Skłodowska-Curie Actions and ERC (European Union); A*MIDEX, ANR, IPhU and Labex P2IO, and Région Auvergne-Rhône-Alpes (France); Key Research Program of Frontier Sciences of CAS, CAS PIFI, CAS CCEPP, Fundamental Research Funds for the Central Universities, and Sci. & Tech. Program of Guangzhou (China); RFBR, RSF and Yandex LLC (Russia); GVA, XuntaGal and GENCAT (Spain); the Leverhulme Trust, the Royal Society and UKRI (United Kingdom).

References

- [1] M.L. Miller, K. Reygers, S.J. Sanders and P. Steinberg, *Glauber modeling in high energy nuclear collisions*, *Ann. Rev. Nucl. Part. Sci.* **57** (2007) 205 [[nucl-ex/0701025](https://arxiv.org/abs/nucl-ex/0701025)].
- [2] ALICE collaboration, *Centrality dependence of the charged-particle multiplicity density at midrapidity in Pb-Pb collisions at $\sqrt{s_{NN}} = 5.02$ TeV*, *Phys. Rev. Lett.* **116** (2016) 222302 [[arXiv:1512.06104](https://arxiv.org/abs/1512.06104)].
- [3] ALICE collaboration, *Centrality dependence of the charged-particle multiplicity density at midrapidity in Pb-Pb collisions at $\sqrt{s_{NN}} = 5.02$ TeV*, *ALICE-PUBLIC-2015-008* (2015).
- [4] ATLAS collaboration, *Measurement of the nuclear modification factor for inclusive jets in Pb+Pb collisions at $\sqrt{s_{NN}} = 5.02$ TeV with the ATLAS detector*, *Phys. Lett. B* **790** (2019) 108 [[arXiv:1805.05635](https://arxiv.org/abs/1805.05635)].
- [5] CMS collaboration, *Constraints on the initial state of Pb-Pb collisions via measurements of Z-boson yields and azimuthal anisotropy at $\sqrt{s_{NN}} = 5.02$ TeV*, *Phys. Rev. Lett.* **127** (2021) 102002 [[arXiv:2103.14089](https://arxiv.org/abs/2103.14089)].
- [6] LHCb collaboration, *The LHCb detector at the LHC*, *2008 JINST* **3** S08005.
- [7] LHCb collaboration, *LHCb detector performance*, *Int. J. Mod. Phys. A* **30** (2015) 1530022 [[arXiv:1412.6352](https://arxiv.org/abs/1412.6352)].
- [8] LHCb collaboration, *Precision luminosity measurements at LHCb*, *2014 JINST* **9** P12005 [[arXiv:1410.0149](https://arxiv.org/abs/1410.0149)].
- [9] ALICE collaboration, *Measurement of the cross section for electromagnetic dissociation with neutron emission in Pb-Pb collisions at $\sqrt{s_{NN}} = 2.76$ TeV*, *Phys. Rev. Lett.* **109** (2012) 252302 [[arXiv:1203.2436](https://arxiv.org/abs/1203.2436)].
- [10] *Nuclear data services*, <https://www-nds.iaea.org/radii/>, last accessed: 2020-11-04.
- [11] I. Angeli and K.P. Marinova, *Table of experimental nuclear ground state charge radii: An update*, *Atom. Data Nucl. Data Tabl.* **99** (2013) 69.
- [12] C. Loizides, J. Nagle and P. Steinberg, *Improved version of the PHOBOS Glauber Monte Carlo, SoftwareX* **1-2** (2015) 13 [[arXiv:1408.2549](https://arxiv.org/abs/1408.2549)].
- [13] C. Loizides, J. Kamin and D. d'Enterria, *Improved Monte Carlo Glauber predictions at present and future nuclear colliders*, *Phys. Rev. C* **97** (2018) 054910 [*Erratum ibid.* **99** (2019) 019901] [[arXiv:1710.07098](https://arxiv.org/abs/1710.07098)].
- [14] S. Hatakeyama, W. Horiuchi and A. Kohama, *Nuclear surface diffuseness revealed in nucleon-nucleus diffraction*, *Phys. Rev. C* **97** (2018) 054607 [[arXiv:1805.03325](https://arxiv.org/abs/1805.03325)].
- [15] A. Bohr and B.R. Mottelson, *Nuclear structure*, World Scientific Publishing Company, Singapore (1998) [[DOI](https://doi.org/10.1142/2133)].
- [16] W.M. Seif and H. Mansour, *Systematics of nucleon density distributions and neutron skin of nuclei*, *Int. J. Mod. Phys. E* **24** (2015) 1550083 [[arXiv:1504.08350](https://arxiv.org/abs/1504.08350)].
- [17] L. Durand and P. Hong, *QCD and rising cross sections*, *Phys. Rev. Lett.* **58** (1987) 303.
- [18] W.R. Chen, R.C. Hwa and X.-n. Wang, *Particle productivity in pp and pA collisions*, *Phys. Rev. D* **38** (1988) 3394.
- [19] W.R. Chen and R.C. Hwa, *Geometrical branching model: Phenomenology with jets*, *Phys. Rev. D* **39** (1989) 179.

- [20] X.-N. Wang, *Role of multiple minijets in high-energy hadronic reactions*, *Phys. Rev. D* **43** (1991) 104.
- [21] W.-T. Deng, X.-N. Wang and R. Xu, *Hadron production in $p + p$, $p + Pb$, and $Pb + Pb$ collisions with the hijing 2.0 model at energies available at the CERN Large Hadron Collider*, *Phys. Rev. C* **83** (2011) 014915 [[arXiv:1008.1841](https://arxiv.org/abs/1008.1841)].
- [22] J. Cugnon and O. Harouna, *Validity of the negative binomial distribution in particle production*, *EPL* **4** (1987) 1127.
- [23] P. Ghosh, *Negative binomial multiplicity distribution in proton-proton collisions in limited pseudorapidity intervals at LHC up to $\sqrt{s} = 7$ TeV and the clan model*, *Phys. Rev. D* **85** (2012) 054017 [[arXiv:1202.4221](https://arxiv.org/abs/1202.4221)].
- [24] ALICE collaboration, *Charged-particle multiplicity measurement in proton-proton collisions at $\sqrt{s} = 0.9$ and 2.36 TeV with ALICE at LHC*, *Eur. Phys. J. C* **68** (2010) 89 [[arXiv:1004.3034](https://arxiv.org/abs/1004.3034)].
- [25] ALICE collaboration, *Charged-particle multiplicity measurement in proton-proton collisions at $\sqrt{s} = 7$ TeV with ALICE at LHC*, *Eur. Phys. J. C* **68** (2010) 345 [[arXiv:1004.3514](https://arxiv.org/abs/1004.3514)].
- [26] LHCb collaboration, *Measurement of charged particle multiplicities and densities in pp collisions at $\sqrt{s} = 7$ TeV in the forward region*, *Eur. Phys. J. C* **74** (2014) 2888 [[arXiv:1402.4430](https://arxiv.org/abs/1402.4430)].
- [27] ALICE collaboration, *Centrality determination of $Pb-Pb$ collisions at $\sqrt{s_{NN}} = 2.76$ TeV with ALICE*, *Phys. Rev. C* **88** (2013) 044909 [[arXiv:1301.4361](https://arxiv.org/abs/1301.4361)].

The LHCb collaboration

R. Aaij,³² C. Abellán Beteta,⁵⁰ T. Ackernley,⁶⁰ B. Adeva,⁴⁶ M. Adinolfi,⁵⁴ H. Afsharnia,⁹ C.A. Aidala,⁸⁵ S. Aiola,²⁵ Z. Ajaltouni,⁹ S. Akar,⁶⁵ J. Albrecht,¹⁵ F. Alessio,⁴⁸ M. Alexander,⁵⁹ A. Alfonso Albero,⁴⁵ Z. Aliouche,⁶² G. Alkhazov,³⁸ P. Alvarez Cartelle,⁵⁵ S. Amato,² Y. Amhis,¹¹ L. An,⁴⁸ L. Anderlini,²² A. Andreianov,³⁸ M. Andreotti,²¹ F. Archilli,¹⁷ A. Artamonov,⁴⁴ M. Artuso,⁶⁸ K. Arzimatov,⁴² E. Aslanides,¹⁰ M. Atzeni,⁵⁰ B. Audurier,¹² S. Bachmann,¹⁷ M. Bachmayer,⁴⁹ J.J. Back,⁵⁶ P. Baladron Rodriguez,⁴⁶ V. Balagura,¹² W. Baldini,²¹ J. Baptista Leite,¹ R.J. Barlow,⁶² S. Barsuk,¹¹ W. Barter,⁶¹ M. Bartolini,^{24,h} F. Baryshnikov,⁸² J.M. Basels,¹⁴ G. Bassi,²⁹ B. Batsukh,⁶⁸ A. Battig,¹⁵ A. Bay,⁴⁹ M. Becker,¹⁵ F. Bedeschi,²⁹ I. Bediaga,¹ A. Beiter,⁶⁸ V. Belavin,⁴² S. Belin,²⁷ V. Bellee,⁴⁹ K. Belous,⁴⁴ I. Belov,⁴⁰ I. Belyaev,⁴¹ G. Bencivenni,²³ E. Ben-Haim,¹³ A. Berezhnoy,⁴⁰ R. Bernet,⁵⁰ D. Berninghoff,¹⁷ H.C. Bernstein,⁶⁸ C. Bertella,⁴⁸ A. Bertolin,²⁸ C. Betancourt,⁵⁰ F. Betti,⁴⁸ Ia. Bezshyiko,⁵⁰ S. Bhasin,⁵⁴ J. Bhom,³⁵ L. Bian,⁷³ M.S. Bieker,¹⁵ S. Bifani,⁵³ P. Billoir,¹³ M. Birch,⁶¹ F.C.R. Bishop,⁵⁵ A. Bitadze,⁶² A. Bizzeti,^{22,k} M. Bjørn,⁶³ M.P. Blago,⁴⁸ T. Blake,⁵⁶ F. Blanc,⁴⁹ S. Blusk,⁶⁸ D. Bobulska,⁵⁹ J.A. Boelhauve,¹⁵ O. Boente Garcia,⁴⁶ T. Boettcher,⁶⁵ A. Boldyrev,⁸¹ A. Bondar,⁴³ N. Bondar,^{38,48} S. Borghi,⁶² M. Borisyak,⁴² M. Borsato,¹⁷ J.T. Borsuk,³⁵ S.A. Bouchiba,⁴⁹ T.J.V. Bowcock,⁶⁰ A. Boyer,⁴⁸ C. Bozzi,²¹ M.J. Bradley,⁶¹ S. Braun,⁶⁶ A. Brea Rodriguez,⁴⁶ M. Brodski,⁴⁸ J. Brodzicka,³⁵ A. Brossa Gonzalo,⁵⁶ D. Brundu,²⁷ A. Buonaura,⁵⁰ C. Burr,⁴⁸ A. Bursche,⁷² A. Butkevich,³⁹ J.S. Butter,³² J. Buytaert,⁴⁸ W. Byczynski,⁴⁸ S. Cadeddu,²⁷ H. Cai,⁷³ R. Calabrese,^{21,f} L. Calefice,^{15,13} L. Calero Diaz,²³ S. Cali,²³ R. Calladine,⁵³ M. Calvi,^{26,j} M. Calvo Gomez,⁸⁴ P. Camargo Magalhaes,⁵⁴ A. Camboni,^{45,84} P. Campana,²³ A.F. Campoverde Quezada,⁶ S. Capelli,^{26,j} L. Capriotti,^{20,d} A. Carbone,^{20,d} G. Carboni,³¹ R. Cardinale,^{24,h} A. Cardini,²⁷ I. Carli,⁴ P. Carniti,^{26,j} L. Carus,¹⁴ K. Carvalho Akiba,³² A. Casais Vidal,⁴⁶ G. Casse,⁶⁰ M. Cattaneo,⁴⁸ G. Cavallero,⁴⁸ S. Celani,⁴⁹ J. Cerasoli,¹⁰ A.J. Chadwick,⁶⁰ M.G. Chapman,⁵⁴ M. Charles,¹³ Ph. Charpentier,⁴⁸ G. Chatzikonstantinidis,⁵³ C.A. Chavez Barajas,⁶⁰ M. Chefdeville,⁸ C. Chen,³ S. Chen,⁴ A. Chernov,³⁵ V. Chobanova,⁴⁶ S. Cholak,⁴⁹ M. Chrzaszcz,³⁵ A. Chubykin,³⁸ V. Chulikov,³⁸ P. Ciambrone,²³ M.F. Cicala,⁵⁶ X. Cid Vidal,⁴⁶ G. Ciezarek,⁴⁸ P.E.L. Clarke,⁵⁸ M. Clemencic,⁴⁸ H.V. Cliff,⁵⁵ J. Closier,⁴⁸ J.L. Cobbledick,⁶² V. Coco,⁴⁸ J.A.B. Coelho,¹¹ J. Cogan,¹⁰ E. Cogneras,⁹ L. Cojocariu,³⁷ P. Collins,⁴⁸ T. Colombo,⁴⁸ L. Congedo,^{19,c} A. Contu,²⁷ N. Cooke,⁵³ G. Coombs,⁵⁹ G. Corti,⁴⁸ C.M. Costa Sobral,⁵⁶ B. Couturier,⁴⁸ D.C. Craik,⁶⁴ J. Crkovská,⁶⁷ M. Cruz Torres,¹ R. Currie,⁵⁸ C.L. Da Silva,⁶⁷ E. Dall'Occo,¹⁵ J. Dalseno,⁴⁶ C. D'Ambrosio,⁴⁸ A. Danilina,⁴¹ P. d'Argent,⁴⁸ A. Davis,⁶² O. De Aguiar Francisco,⁶² K. De Bruyn,⁷⁸ S. De Capua,⁶² M. De Cian,⁴⁹ J.M. De Miranda,¹ L. De Paula,² M. De Serio,^{19,c} D. De Simone,⁵⁰ P. De Simone,²³ J.A. de Vries,⁷⁹ C.T. Dean,⁶⁷ D. Decamp,⁸ L. Del Buono,¹³ B. Delaney,⁵⁵ H.-P. Dembinski,¹⁵ A. Dendek,³⁴ V. Denysenko,⁵⁰ D. Derkach,⁸¹ O. Deschamps,⁹ F. Desse,¹¹ F. Dettori,^{27,e} B. Dey,⁷³ P. Di Nezza,²³ S. Didenko,⁸² L. Dieste Maronas,⁴⁶ H. Dijkstra,⁴⁸ V. Dobishuk,⁵² A.M. Donohoe,¹⁸ F. Dordei,²⁷ A.C. dos Reis,¹ L. Douglas,⁵⁹ A. Dovbnya,⁵¹ A.G. Downes,⁸ K. Dreimanis,⁶⁰ M.W. Dudek,³⁵ L. Dufour,⁴⁸ V. Duk,⁷⁷ P. Durante,⁴⁸ J.M. Durham,⁶⁷ D. Dutta,⁶² A. Dziurda,³⁵ A. Dzyuba,³⁸ S. Easo,⁵⁷ U. Egede,⁶⁹ V. Egorychev,⁴¹ S. Eidelman,^{43,v} S. Eisenhardt,⁵⁸ S. Ek-In,⁴⁹ L. Eklund,^{59,w} S. Ely,⁶⁸ A. Ene,³⁷ E. Epple,⁶⁷ S. Escher,¹⁴ J. Eschle,⁵⁰ S. Esen,¹³ T. Evans,⁴⁸ A. Falabella,²⁰ J. Fan,³ Y. Fan,⁶ B. Fang,⁷³ S. Farry,⁶⁰ D. Fazzini,^{26,j} M. Féo,⁴⁸ A. Fernandez Prieto,⁴⁶ A.D. Fernez,⁶⁶ F. Ferrari,^{20,d} L. Ferreira Lopes,⁴⁹ F. Ferreira Rodrigues,² S. Ferreres Sole,³² M. Ferrillo,⁵⁰ M. Ferro-Luzzi,⁴⁸ S. Filippov,³⁹ R.A. Fini,¹⁹ M. Fiorini,^{21,f} M. Firlej,³⁴ K.M. Fischer,⁶³ D.S. Fitzgerald,⁸⁵ C. Fitzpatrick,⁶² T. Fiutowski,³⁴ F. Fleuret,¹² M. Fontana,¹³ F. Fontanelli,^{24,h} R. Forty,⁴⁸ V. Franco Lima,⁶⁰ M. Franco Sevilla,⁶⁶ M. Frank,⁴⁸ E. Franzoso,²¹ G. Frau,¹⁷ C. Frei,⁴⁸ D.A. Friday,⁵⁹ J. Fu,²⁵ Q. Fuehring,¹⁵ W. Funk,⁴⁸ E. Gabriel,³² T. Gaintseva,⁴² A. Gallas Torreira,⁴⁶ D. Galli,^{20,d} S. Gambetta,^{58,48} Y. Gan,³ M. Gandelman,² P. Gandini,²⁵ Y. Gao,⁵ M. Garau,²⁷ L.M. Garcia Martin,⁵⁶ P. Garcia Moreno,⁴⁵ J. Garcia Pardiñas,^{26,j} B. Garcia Plana,⁴⁶ F.A. Garcia Rosales,¹² L. Garrido,⁴⁵ C. Gaspar,⁴⁸ R.E. Geertsema,³² D. Gerick,¹⁷ L.L. Gerken,¹⁵

E. Gersabeck,⁶² M. Gersabeck,⁶² T. Gershon,⁵⁶ D. Gerstel,¹⁰ Ph. Ghez,⁸ V. Gibson,⁵⁵ H.K. Giemza,³⁶
 M. Giovannetti,^{23,p} A. Gioventù,⁴⁶ P. Gironella Gironell,⁴⁵ L. Giubega,³⁷ C. Giugliano,^{21,f,48}
 K. Gizzdov,⁵⁸ E.L. Gkougkousis,⁴⁸ V.V. Gligorov,¹³ C. Göbel,⁷⁰ E. Golobardes,⁸⁴ D. Golubkov,⁴¹
 A. Golutvin,^{61,82} A. Gomes,^{1,a} S. Gomez Fernandez,⁴⁵ F. Goncalves Abrantes,⁶³ M. Goncerz,³⁵ G. Gong,³
 P. Gorbounov,⁴¹ I.V. Gorelov,⁴⁰ C. Gotti,²⁶ E. Govorkova,⁴⁸ J.P. Grabowski,¹⁷ T. Grammatico,¹³
 L.A. Granado Cardoso,⁴⁸ E. Graugés,⁴⁵ E. Graverini,⁴⁹ G. Graziani,²² A. Grecu,³⁷ L.M. Greeven,³²
 P. Griffith,^{21,f} L. Grillo,⁶² S. Gromov,⁸² B.R. Gruberg Cazon,⁶³ C. Gu,³ M. Guarise,²¹ P.A. Günther,¹⁷
 E. Gushchin,³⁹ A. Guth,¹⁴ Y. Guz,⁴⁴ T. Gys,⁴⁸ T. Hadavizadeh,⁶⁹ G. Haefeli,⁴⁹ C. Haen,⁴⁸
 J. Haimberger,⁴⁸ T. Halewood-leagas,⁶⁰ P.M. Hamilton,⁶⁶ Q. Han,⁷ X. Han,¹⁷ T.H. Hancock,⁶³
 S. Hansmann-Menzemer,¹⁷ N. Harnew,⁶³ T. Harrison,⁶⁰ C. Hasse,⁴⁸ M. Hatch,⁴⁸ J. He,^{6,b} M. Hecker,⁶¹
 K. Heijhoff,³² K. Heinicke,¹⁵ A.M. Hennequin,⁴⁸ K. Hennessy,⁶⁰ L. Henry,^{25,47} J. Heuel,¹⁴ A. Hicheur,²
 D. Hill,⁴⁹ M. Hilton,⁶² S.E. Hollitt,¹⁵ J. Hu,¹⁷ J. Hu,⁷² W. Hu,⁷ W. Huang,⁶ X. Huang,⁷³
 W. Hulsbergen,³² R.J. Hunter,⁵⁶ M. Hushchyn,⁸¹ D. Hutchcroft,⁶⁰ D. Hynds,³² P. Ibis,¹⁵ M. Idzik,³⁴
 D. Ilin,³⁸ P. Ilten,⁶⁵ A. Inglessi,³⁸ A. Ishteev,⁸² K. Ivshin,³⁸ R. Jacobsson,⁴⁸ S. Jakobsen,⁴⁸ E. Jans,³²
 B.K. Jashal,⁴⁷ A. Jawahery,⁶⁶ V. Jevtic,¹⁵ F. Jiang,³ M. John,⁶³ D. Johnson,⁴⁸ C.R. Jones,⁵⁵ T.P. Jones,⁵⁶
 B. Jost,⁴⁸ N. Jurik,⁴⁸ S. Kandybei,⁵¹ Y. Kang,³ M. Karacson,⁴⁸ M. Karpov,⁸¹ F. Keizer,⁴⁸ M. Kenzie,⁵⁶
 T. Ketel,³³ B. Khanji,¹⁵ A. Kharisova,⁸³ S. Kholodenko,⁴⁴ T. Kirn,¹⁴ V.S. Kirsebom,⁴⁹ O. Kitouni,⁶⁴
 S. Klaver,³² K. Klimaszewski,³⁶ S. Koliiev,⁵² A. Kondybayeva,⁸² A. Konoplyannikov,⁴¹ P. Kopciewicz,³⁴
 R. Kopecna,¹⁷ P. Koppenburg,³² M. Korolev,⁴⁰ I. Kostiuk,^{32,52} O. Kot,⁵² S. Kotriakhova,^{21,38}
 P. Kravchenko,³⁸ L. Kravchuk,³⁹ R.D. Krawczyk,⁴⁸ M. Kreps,⁵⁶ F. Kress,⁶¹ S. Kretzschmar,¹⁴
 P. Krokovny,^{43,v} W. Krupa,³⁴ W. Krzemien,³⁶ W. Kucewicz,^{35,t} M. Kucharczyk,³⁵ V. Kudryavtsev,^{43,v}
 H.S. Kuindersma,^{32,33} G.J. Kunde,⁶⁷ T. Kvaratskheliya,⁴¹ D. Lacarrere,⁴⁸ G. Lafferty,⁶² A. Lai,²⁷
 A. Lampis,²⁷ D. Lancierini,⁵⁰ J.J. Lane,⁶² R. Lane,⁵⁴ G. Lanfranchi,²³ C. Langenbruch,¹⁴ J. Langer,¹⁵
 O. Lantwin,⁵⁰ T. Latham,⁵⁶ F. Lazzari,^{29,q} R. Le Gac,¹⁰ S.H. Lee,⁸⁵ R. Lefèvre,⁹ A. Leflat,⁴⁰
 S. Legotin,⁸² O. Leroy,¹⁰ T. Lesiak,³⁵ B. Leverington,¹⁷ H. Li,⁷² L. Li,⁶³ P. Li,¹⁷ S. Li,⁷ Y. Li,⁴ Y. Li,⁴
 Z. Li,⁶⁸ X. Liang,⁶⁸ T. Lin,⁶¹ R. Lindner,⁴⁸ V. Lisovskyi,¹⁵ R. Litvinov,²⁷ G. Liu,⁷² H. Liu,⁶ S. Liu,⁴
 X. Liu,³ A. Loi,²⁷ J. Lomba Castro,⁴⁶ I. Longstaff,⁵⁹ J.H. Lopes,² G.H. Lovell,⁵⁵ Y. Lu,⁴ D. Lucchesi,^{28,l}
 S. Luchuk,³⁹ M. Lucio Martinez,³² V. Lukashenko,^{32,52} Y. Luo,³ A. Lupato,⁶² E. Luppi,^{21,f} O. Lupton,⁵⁶
 A. Lusiani,^{29,m} X. Lyu,⁶ L. Ma,⁴ R. Ma,⁶ S. Maccolini,^{20,d} F. Machefert,¹¹ F. Maciuc,³⁷ V. Macko,⁴⁹
 P. Mackowiak,¹⁵ S. Maddrell-Mander,⁵⁴ O. Madejczyk,³⁴ L.R. Madhan Mohan,⁵⁴ O. Maev,³⁸
 A. Maevskiy,⁸¹ D. Maisuzenko,³⁸ M.W. Majewski,³⁴ J.J. Malczewski,³⁵ S. Malde,⁶³ B. Malecki,⁴⁸
 A. Malinin,⁸⁰ T. Maltsev,^{43,v} H. Malygina,¹⁷ G. Manca,^{27,e} G. Mancinelli,¹⁰ D. Manuzzi,^{20,d}
 D. Marangotto,^{25,i} J. Maratas,^{9,s} J.F. Marchand,⁸ U. Marconi,²⁰ S. Mariani,^{22,g} C. Marin Benito,⁴⁸
 M. Marinangeli,⁴⁹ J. Marks,¹⁷ A.M. Marshall,⁵⁴ P.J. Marshall,⁶⁰ G. Martellotti,³⁰ L. Martinazzoli,^{48,j}
 M. Martinelli,^{26,j} D. Martinez Santos,⁴⁶ F. Martinez Vidal,⁴⁷ A. Massafferri,¹ M. Materok,¹⁴ R. Matev,⁴⁸
 A. Mathad,⁵⁰ Z. Mathe,⁴⁸ V. Matiunin,⁴¹ C. Matteuzzi,²⁶ K.R. Mattioli,⁸⁵ A. Mauri,³² E. Maurice,¹²
 J. Mauricio,⁴⁵ M. Mazurek,⁴⁸ M. McCann,⁶¹ L. Mcconnell,¹⁸ T.H. McGrath,⁶² A. McNab,⁶²
 R. McNulty,¹⁸ J.V. Mead,⁶⁰ B. Meadows,⁶⁵ C. Meaux,¹⁰ G. Meier,¹⁵ N. Meinert,⁷⁶ D. Melnychuk,³⁶
 S. Meloni,^{26,j} M. Merk,^{32,79} A. Merli,²⁵ L. Meyer Garcia,² M. Mikhasenko,⁴⁸ D.A. Milanes,⁷⁴
 E. Millard,⁵⁶ M. Milovanovic,⁴⁸ M.-N. Minard,⁸ A. Minotti,²¹ L. Minzoni,^{21,f} S.E. Mitchell,⁵⁸
 B. Mitreska,⁶² D.S. Mitzel,⁴⁸ A. Mödden,¹⁵ R.A. Mohammed,⁶³ R.D. Moise,⁶¹ T. Mombächer,¹⁵
 I.A. Monroy,⁷⁴ S. Monteil,⁹ M. Morandin,²⁸ G. Morello,²³ M.J. Morello,^{29,m} J. Moron,³⁴ A.B. Morris,⁷⁵
 A.G. Morris,⁵⁶ R. Mountain,⁶⁸ H. Mu,³ F. Muheim,^{58,48} M. Mulder,⁴⁸ D. Müller,⁴⁸ K. Müller,⁵⁰
 C.H. Murphy,⁶³ D. Murray,⁶² P. Muzzetto,^{27,48} P. Naik,⁵⁴ T. Nakada,⁴⁹ R. Nandakumar,⁵⁷ T. Nanut,⁴⁹
 I. Nasteva,² M. Needham,⁵⁸ I. Neri,²¹ N. Neri,^{25,i} S. Neubert,⁷⁵ N. Neufeld,⁴⁸ R. Newcombe,⁶¹
 T.D. Nguyen,⁴⁹ C. Nguyen-Mau,^{49,x} E.M. Niel,¹¹ S. Nieswand,¹⁴ N. Nikitin,⁴⁰ N.S. Nolte,¹⁵ C. Nunez,⁸⁵
 A. Oblakowska-Mucha,³⁴ V. Obraztsov,⁴⁴ D.P. O'Hanlon,⁵⁴ R. Oldeman,^{27,e} M.E. Olivares,⁶⁸
 C.J.G. Onderwater,⁷⁸ A. Ossowska,³⁵ J.M. Otalora Goicochea,² T. Ovsiannikova,⁴¹ P. Owen,⁵⁰

A. Oyanguren,⁴⁷ B. Pagare,⁵⁶ P.R. Pais,⁴⁸ T. Pajero,⁶³ A. Palano,¹⁹ M. Palutan,²³ Y. Pan,⁶² G. Panshin,⁸³
 A. Papanestis,⁵⁷ M. Pappagallo,^{19,c} L.L. Pappalardo,^{21,f} C. Pappenheimer,⁶⁵ W. Parker,⁶⁶ C. Parkes,⁶²
 C.J. Parkinson,⁴⁶ B. Passalacqua,²¹ G. Passaleva,²² A. Pastore,¹⁹ M. Patel,⁶¹ C. Patrignani,^{20,d}
 C.J. Pawley,⁷⁹ A. Pearce,⁴⁸ A. Pellegrino,³² M. Pepe Altarelli,⁴⁸ S. Perazzini,²⁰ D. Pereima,⁴¹ P. Perret,⁹
 M. Petric,^{59,48} K. Petridis,⁵⁴ A. Petrolini,^{24,h} A. Petrov,⁸⁰ S. Petrucci,⁵⁸ M. Petruzzo,²⁵ T.T.H. Pham,⁶⁸
 A. Philippov,⁴² L. Pica,^{29,m} M. Piccini,⁷⁷ B. Pietrzyk,⁸ G. Pietrzyk,⁴⁹ M. Pili,⁶³ D. Pinci,³⁰ F. Pisani,⁴⁸
 P.K. Resmi,¹⁰ V. Placinta,³⁷ J. Plews,⁵³ M. Plo Casasus,⁴⁶ F. Polci,¹³ M. Poli Lener,²³ M. Poliakova,⁶⁸
 A. Poluektov,¹⁰ N. Polukhina,^{82,u} I. Polyakov,⁶⁸ E. Polycarpo,² G.J. Pomery,⁵⁴ S. Ponce,⁴⁸ D. Popov,^{6,48}
 S. Popov,⁴² S. Poslavskii,⁴⁴ K. Prasanth,³⁵ L. Promberger,⁴⁸ C. Prouve,⁴⁶ V. Pugatch,⁵² H. Pullen,⁶³
 G. Punzi,^{29,n} W. Qian,⁶ J. Qin,⁶ R. Quagliani,¹³ B. Quintana,⁸ N.V. Raab,¹⁸ R.I. Rabadan Trejo,¹⁰
 B. Rachwal,³⁴ J.H. Rademacker,⁵⁴ M. Rama,²⁹ M. Ramos Pernas,⁵⁶ M.S. Rangel,² F. Ratnikov,^{42,81}
 G. Raven,³³ M. Reboud,⁸ F. Redi,⁴⁹ F. Reiss,⁶² C. Remon Alepuz,⁴⁷ Z. Ren,³ V. Renaudin,⁶³ R. Ribatti,²⁹
 S. Ricciardi,⁵⁷ K. Rinnert,⁶⁰ P. Robbe,¹¹ G. Robertson,⁵⁸ A.B. Rodrigues,⁴⁹ E. Rodrigues,⁶⁰
 J.A. Rodriguez Lopez,⁷⁴ A. Rollings,⁶³ P. Roloff,⁴⁸ V. Romanovskiy,⁴⁴ M. Romero Lamas,⁴⁶
 A. Romero Vidal,⁴⁶ J.D. Roth,⁸⁵ M. Rotondo,²³ M.S. Rudolph,⁶⁸ T. Ruf,⁴⁸ J. Ruiz Vidal,⁴⁷ A. Ryzhikov,⁸¹
 J. Ryzka,³⁴ J.J. Saborido Silva,⁴⁶ N. Sagidova,³⁸ N. Sahoo,⁵⁶ B. Saitta,^{27,e} M. Salomoni,⁴⁸
 C. Sanchez Gras,³² R. Santacesaria,³⁰ C. Santamarina Rios,⁴⁶ M. Santimaria,²³ E. Santovetti,^{31,p}
 D. Saranin,⁸² G. Sarpis,¹⁴ M. Sarpis,⁷⁵ A. Sarti,³⁰ C. Satriano,^{30,o} A. Satta,³¹ M. Saur,¹⁵ D. Savrina,^{41,40}
 H. Sazak,⁹ L.G. Scantlebury Smead,⁶³ S. Schael,¹⁴ M. Schellenberg,¹⁵ M. Schiller,⁵⁹ H. Schindler,⁴⁸
 M. Schmelling,¹⁶ B. Schmidt,⁴⁸ O. Schneider,⁴⁹ A. Schopper,⁴⁸ M. Schubiger,³² S. Schulte,⁴⁹
 M.H. Schune,¹¹ R. Schwemmer,⁴⁸ B. Sciascia,²³ S. Sellam,⁴⁶ A. Semennikov,⁴¹ M. Senghi Soares,³³
 A. Sergi,^{24,h} N. Serra,⁵⁰ L. Sestini,²⁸ A. Seuthe,¹⁵ P. Seyfert,⁴⁸ Y. Shang,⁵ D.M. Shangase,⁸⁵
 M. Shapkin,⁴⁴ I. Shchemberov,⁸² L. Shchutska,⁴⁹ T. Shears,⁶⁰ L. Shekhtman,^{43,v} Z. Shen,⁵
 V. Shevchenko,⁸⁰ E.B. Shields,^{26,j} E. Shmanin,⁸² J.D. Shupperd,⁶⁸ B.G. Siddi,²¹ R. Silva Coutinho,⁵⁰
 G. Simi,²⁸ S. Simone,^{19,c} N. Skidmore,⁶² T. Skwarnicki,⁶⁸ M.W. Slater,⁵³ I. Slazyk,^{21,f}
 J.C. Smallwood,⁶³ J.G. Smeaton,⁵⁵ A. Smetkina,⁴¹ E. Smith,⁵⁰ M. Smith,⁶¹ A. Snoch,³² M. Soares,²⁰
 L. Soares Lavra,⁹ M.D. Sokoloff,⁶⁵ F.J.P. Soler,⁵⁹ A. Solovev,³⁸ I. Solovyev,³⁸ F.L. Souza De Almeida,²
 B. Souza De Paula,² B. Spaan,¹⁵ E. Spadaro Norella,^{25,i} P. Spradlin,⁵⁹ F. Stagni,⁴⁸ M. Stahl,⁶⁵ S. Stahl,⁴⁸
 P. Steffko,⁴⁹ O. Steinkamp,^{50,82} O. Stenyakin,⁴⁴ H. Stevens,¹⁵ S. Stone,^{68,48} M.E. Stramaglia,⁴⁹
 M. Straticiuc,³⁷ D. Strekalina,⁸² F. Suljik,⁶³ J. Sun,²⁷ L. Sun,⁷³ Y. Sun,⁶⁶ P. Svihra,⁶² P.N. Swallow,⁵³
 K. Swientek,³⁴ A. Szabelski,³⁶ T. Szumlak,³⁴ M. Szymanski,⁴⁸ S. Taneja,⁶² F. Teubert,⁴⁸ E. Thomas,⁴⁸
 K.A. Thomson,⁶⁰ V. Tisserand,⁹ S. T'Jampens,⁸ M. Tobin,⁴ L. Tomassetti,^{21,f} D. Torres Machado,¹
 D.Y. Tou,¹³ M.T. Tran,⁴⁹ E. Trifonova,⁸² C. Tripli,⁴⁹ G. Tuci,^{29,n} A. Tully,⁴⁹ N. Tuning,^{32,48} A. Ukleja,³⁶
 D.J. Unverzagt,¹⁷ E. Ursov,⁸² A. Usachov,³² A. Ustyuzhanin,^{42,81} U. Uwer,¹⁷ A. Vagner,⁸³ V. Vagnoni,²⁰
 A. Valassi,⁴⁸ G. Valenti,²⁰ N. Valls Canudas,⁸⁴ M. van Beuzekom,³² M. Van Dijk,⁴⁹ E. van Herwijnen,⁸²
 C.B. Van Hulse,¹⁸ M. van Veghel,⁷⁸ R. Vazquez Gomez,⁴⁶ P. Vazquez Regueiro,⁴⁶ C. Vázquez Sierra,⁴⁸
 S. Vecchi,²¹ J.J. Velthuis,⁵⁴ M. Veltri,^{22,r} A. Venkateswaran,⁶⁸ M. Veronesi,³² M. Vesterinen,⁵⁶
 D. Vieira,⁶⁵ M. Vieites Diaz,⁴⁹ H. Viemann,⁷⁶ X. Vilasis-Cardona,⁸⁴ E. Vilella Figueras,⁶⁰ P. Vincent,¹³
 D. Vom Bruch,¹⁰ A. Vorobyev,³⁸ V. Vorobyev,^{43,v} N. Voropaev,³⁸ R. Waldi,¹⁷ J. Walsh,²⁹ C. Wang,¹⁷
 J. Wang,⁵ J. Wang,⁴ J. Wang,³ J. Wang,⁷³ M. Wang,³ R. Wang,⁵⁴ Y. Wang,⁷ Z. Wang,⁵⁰ Z. Wang,³
 H.M. Wark,⁶⁰ N.K. Watson,⁵³ S.G. Weber,¹³ D. Websdale,⁶¹ C. Weisser,⁶⁴ B.D.C. Westhenry,⁵⁴
 D.J. White,⁶² M. Whitehead,⁵⁴ D. Wiedner,¹⁵ G. Wilkinson,⁶³ M. Wilkinson,⁶⁸ I. Williams,⁵⁵
 M. Williams,⁶⁴ M.R.J. Williams,⁵⁸ F.F. Wilson,⁵⁷ W. Wislicki,³⁶ M. Witek,³⁵ L. Witola,¹⁷ G. Wormser,¹¹
 S.A. Wotton,⁵⁵ H. Wu,⁶⁸ K. Wyllie,⁴⁸ Z. Xiang,⁶ D. Xiao,⁷ Y. Xie,⁷ A. Xu,⁵ J. Xu,⁶ L. Xu,³ M. Xu,⁷
 Q. Xu,⁶ Z. Xu,⁵ Z. Xu,⁶ D. Yang,³ S. Yang,⁶ Y. Yang,⁶ Z. Yang,³ Z. Yang,⁶⁶ Y. Yao,⁶⁸ L.E. Yeomans,⁶⁰
 H. Yin,⁷ J. Yu,⁷¹ X. Yuan,⁶⁸ O. Yushchenko,⁴⁴ E. Zaffaroni,⁴⁹ M. Zavertyaev,^{16,u} M. Zdybal,³⁵
 O. Zenaiev,⁴⁸ M. Zeng,³ D. Zhang,⁷ L. Zhang,³ S. Zhang,⁵ Y. Zhang,⁵ Y. Zhang,⁶³ A. Zhelezov,¹⁷
 Y. Zheng,⁶ X. Zhou,⁶ Y. Zhou,⁶ X. Zhu,³ Z. Zhu,⁶ V. Zhukov,^{14,40} J.B. Zonneveld,⁵⁸ Q. Zou,⁴
 S. Zucchelli,^{20,d} D. Zuliani,²⁸ G. Zunica⁶²

- ¹ *Centro Brasileiro de Pesquisas Físicas (CBPF), Rio de Janeiro, Brazil*
- ² *Universidade Federal do Rio de Janeiro (UFRJ), Rio de Janeiro, Brazil*
- ³ *Center for High Energy Physics, Tsinghua University, Beijing, China*
- ⁴ *Institute Of High Energy Physics (IHEP), Beijing, China*
- ⁵ *School of Physics State Key Laboratory of Nuclear Physics and Technology, Peking University, Beijing, China*
- ⁶ *University of Chinese Academy of Sciences, Beijing, China*
- ⁷ *Institute of Particle Physics, Central China Normal University, Wuhan, Hubei, China*
- ⁸ *Univ. Savoie Mont Blanc, CNRS, IN2P3-LAPP, Annecy, France*
- ⁹ *Université Clermont Auvergne, CNRS/IN2P3, LPC, Clermont-Ferrand, France*
- ¹⁰ *Aix Marseille Univ, CNRS/IN2P3, CPPM, Marseille, France*
- ¹¹ *Université Paris-Saclay, CNRS/IN2P3, IJCLab, Orsay, France*
- ¹² *Laboratoire Leprince-Ringuet, CNRS/IN2P3, Ecole Polytechnique, Institut Polytechnique de Paris, Palaiseau, France*
- ¹³ *LPNHE, Sorbonne Université, Paris Diderot Sorbonne Paris Cité, CNRS/IN2P3, Paris, France*
- ¹⁴ *I. Physikalisches Institut, RWTH Aachen University, Aachen, Germany*
- ¹⁵ *Fakultät Physik, Technische Universität Dortmund, Dortmund, Germany*
- ¹⁶ *Max-Planck-Institut für Kernphysik (MPIK), Heidelberg, Germany*
- ¹⁷ *Physikalisches Institut, Ruprecht-Karls-Universität Heidelberg, Heidelberg, Germany*
- ¹⁸ *School of Physics, University College Dublin, Dublin, Ireland*
- ¹⁹ *INFN Sezione di Bari, Bari, Italy*
- ²⁰ *INFN Sezione di Bologna, Bologna, Italy*
- ²¹ *INFN Sezione di Ferrara, Ferrara, Italy*
- ²² *INFN Sezione di Firenze, Firenze, Italy*
- ²³ *INFN Laboratori Nazionali di Frascati, Frascati, Italy*
- ²⁴ *INFN Sezione di Genova, Genova, Italy*
- ²⁵ *INFN Sezione di Milano, Milano, Italy*
- ²⁶ *INFN Sezione di Milano-Bicocca, Milano, Italy*
- ²⁷ *INFN Sezione di Cagliari, Monserrato, Italy*
- ²⁸ *Universita degli Studi di Padova, Universita e INFN, Padova, Padova, Italy*
- ²⁹ *INFN Sezione di Pisa, Pisa, Italy*
- ³⁰ *INFN Sezione di Roma La Sapienza, Roma, Italy*
- ³¹ *INFN Sezione di Roma Tor Vergata, Roma, Italy*
- ³² *Nikhef National Institute for Subatomic Physics, Amsterdam, Netherlands*
- ³³ *Nikhef National Institute for Subatomic Physics and VU University Amsterdam, Amsterdam, Netherlands*
- ³⁴ *AGH — University of Science and Technology, Faculty of Physics and Applied Computer Science, Kraków, Poland*
- ³⁵ *Henryk Niewodniczanski Institute of Nuclear Physics Polish Academy of Sciences, Kraków, Poland*
- ³⁶ *National Center for Nuclear Research (NCBJ), Warsaw, Poland*
- ³⁷ *Horia Hulubei National Institute of Physics and Nuclear Engineering, Bucharest-Magurele, Romania*
- ³⁸ *Petersburg Nuclear Physics Institute NRC Kurchatov Institute (PNPI NRC KI), Gatchina, Russia*
- ³⁹ *Institute for Nuclear Research of the Russian Academy of Sciences (INR RAS), Moscow, Russia*
- ⁴⁰ *Institute of Nuclear Physics, Moscow State University (SINP MSU), Moscow, Russia*
- ⁴¹ *Institute of Theoretical and Experimental Physics NRC Kurchatov Institute (ITEP NRC KI), Moscow, Russia*
- ⁴² *Yandex School of Data Analysis, Moscow, Russia*
- ⁴³ *Budker Institute of Nuclear Physics (SB RAS), Novosibirsk, Russia*
- ⁴⁴ *Institute for High Energy Physics NRC Kurchatov Institute (IHEP NRC KI), Protvino, Russia, Protvino, Russia*
- ⁴⁵ *ICCUB, Universitat de Barcelona, Barcelona, Spain*
- ⁴⁶ *Instituto Galego de Física de Altas Enerxías (IGFAE), Universidade de Santiago de Compostela, Santiago de Compostela, Spain*
- ⁴⁷ *Instituto de Fisica Corpuscular, Centro Mixto Universidad de Valencia — CSIC, Valencia, Spain*
- ⁴⁸ *European Organization for Nuclear Research (CERN), Geneva, Switzerland*
- ⁴⁹ *Institute of Physics, Ecole Polytechnique Fédérale de Lausanne (EPFL), Lausanne, Switzerland*
- ⁵⁰ *Physik-Institut, Universität Zürich, Zürich, Switzerland*

⁵¹ NSC Kharkiv Institute of Physics and Technology (NSC KIPT), Kharkiv, Ukraine
⁵² Institute for Nuclear Research of the National Academy of Sciences (KINR), Kyiv, Ukraine
⁵³ University of Birmingham, Birmingham, United Kingdom
⁵⁴ H.H. Wills Physics Laboratory, University of Bristol, Bristol, United Kingdom
⁵⁵ Cavendish Laboratory, University of Cambridge, Cambridge, United Kingdom
⁵⁶ Department of Physics, University of Warwick, Coventry, United Kingdom
⁵⁷ STFC Rutherford Appleton Laboratory, Didcot, United Kingdom
⁵⁸ School of Physics and Astronomy, University of Edinburgh, Edinburgh, United Kingdom
⁵⁹ School of Physics and Astronomy, University of Glasgow, Glasgow, United Kingdom
⁶⁰ Oliver Lodge Laboratory, University of Liverpool, Liverpool, United Kingdom
⁶¹ Imperial College London, London, United Kingdom
⁶² Department of Physics and Astronomy, University of Manchester, Manchester, United Kingdom
⁶³ Department of Physics, University of Oxford, Oxford, United Kingdom
⁶⁴ Massachusetts Institute of Technology, Cambridge, MA, United States
⁶⁵ University of Cincinnati, Cincinnati, OH, United States
⁶⁶ University of Maryland, College Park, MD, United States
⁶⁷ Los Alamos National Laboratory (LANL), Los Alamos, United States
⁶⁸ Syracuse University, Syracuse, NY, United States
⁶⁹ School of Physics and Astronomy, Monash University, Melbourne, Australia, associated to ⁵⁶
⁷⁰ Pontifícia Universidade Católica do Rio de Janeiro (PUC-Rio), Rio de Janeiro, Brazil, associated to ²
⁷¹ Physics and Micro Electronic College, Hunan University, Changsha City, China, associated to ⁷
⁷² Guangdong Provincial Key Laboratory of Nuclear Science, Guangdong-Hong Kong Joint Laboratory of Quantum Matter, Institute of Quantum Matter, South China Normal University, Guangzhou, China, associated to ³
⁷³ School of Physics and Technology, Wuhan University, Wuhan, China, associated to ³
⁷⁴ Departamento de Física, Universidad Nacional de Colombia, Bogota, Colombia, associated to ¹³
⁷⁵ Universität Bonn — Helmholtz-Institut für Strahlen und Kernphysik, Bonn, Germany, associated to ¹⁷
⁷⁶ Institut für Physik, Universität Rostock, Rostock, Germany, associated to ¹⁷
⁷⁷ INFN Sezione di Perugia, Perugia, Italy, associated to ²¹
⁷⁸ Van Swinderen Institute, University of Groningen, Groningen, Netherlands, associated to ³²
⁷⁹ Universiteit Maastricht, Maastricht, Netherlands, associated to ³²
⁸⁰ National Research Centre Kurchatov Institute, Moscow, Russia, associated to ⁴¹
⁸¹ National Research University Higher School of Economics, Moscow, Russia, associated to ⁴²
⁸² National University of Science and Technology “MISIS”, Moscow, Russia, associated to ⁴¹
⁸³ National Research Tomsk Polytechnic University, Tomsk, Russia, associated to ⁴¹
⁸⁴ DS4DS, La Salle, Universitat Ramon Llull, Barcelona, Spain, associated to ⁴⁵
⁸⁵ University of Michigan, Ann Arbor, United States, associated to ⁶⁸

^a Universidade Federal do Triângulo Mineiro (UFTM), Uberaba-MG, Brazil

^b Hangzhou Institute for Advanced Study, UCAS, Hangzhou, China

^c Università di Bari, Bari, Italy

^d Università di Bologna, Bologna, Italy

^e Università di Cagliari, Cagliari, Italy

^f Università di Ferrara, Ferrara, Italy

^g Università di Firenze, Firenze, Italy

^h Università di Genova, Genova, Italy

ⁱ Università degli Studi di Milano, Milano, Italy

^j Università di Milano Bicocca, Milano, Italy

^k Università di Modena e Reggio Emilia, Modena, Italy

^l Università di Padova, Padova, Italy

^m Scuola Normale Superiore, Pisa, Italy

ⁿ Università di Pisa, Pisa, Italy

^o Università della Basilicata, Potenza, Italy

^p Università di Roma Tor Vergata, Roma, Italy

^q *Università di Siena, Siena, Italy*
^r *Università di Urbino, Urbino, Italy*
^s *MSU — Iligan Institute of Technology (MSU-IIT), Iligan, Philippines*
^t *AGH — University of Science and Technology, Faculty of Computer Science, Electronics and Telecommunications, Kraków, Poland*
^u *P.N. Lebedev Physical Institute, Russian Academy of Science (LPI RAS), Moscow, Russia*
^v *Novosibirsk State University, Novosibirsk, Russia*
^w *Department of Physics and Astronomy, Uppsala University, Uppsala, Sweden*
^x *Hanoi University of Science, Hanoi, Vietnam*